ACS APPLIED NANO MATERIALS

www.acsanm.org Article

Chitosan Nanococktails Containing Both Ceria and Superparamagnetic Iron Oxide Nanoparticles for Reactive Oxygen Species-Related Theranostics

Yuao Wu, Run Zhang, Huong D. N. Tran, Nyoman D. Kurniawan, Shehzahdi S. Moonshi, Andrew K. Whittaker, and Hang T. Ta*

Cite This: https://doi.org/10.1021/acsanm.1c00141 Read Online

ACCESS | Metrics & More | Article Recommendations | Supporting Information

ABSTRACT: Reactive oxygen species (ROS) play an essential role in the progression of many chronic diseases like atherosclerosis and rheumatoid arthritis. For decades, antioxidant compounds have always been considered as potential treatments for these ROS-related diseases. Concomitantly, noninvasive imaging systems such as magnetic resonance imaging (MRI) have also been widely used in the diagnosis of diseases, especially atherosclerosis. In this study, we investigated the feasibility to develop chitosan nanococktails containing both nanoceria and superparamagnetic iron oxide nanoparticles for ROS-related theranostics. Nanoceria utilized as therapeutic modules capable of ROS scavenging and iron-oxide nanoparticles utilized as imaging agents for MRI have been synthesized separately. Subsequently, two versions of theranostic chitosan nanococktails containing both nanoceria and iron oxide nanoparticles (Chit-IOCO and Chit-TPP-IOCO) were successfully synthesized *via* two different mechanisms, electrostatic self-assembly, and ionic gelation. *In vitro* studies such as cytotoxicity, MRI, and ROS scavenging were performed. These theranostic nanococktails demonstrated effective ROS scavenging and MRI contrast as a potential platform for treatment and diagnosis of ROS-related diseases. Results indicated that both Chit-IOCO and Chit-TPP-IOCO can reduce the ROS level of the lipopolysaccharide-stimulated macrophage J774A.1 to the baseline level. Chit-IOCO was less toxic to the cells than Chit-TPP-IOCO. In addition, Chit-IOCO exhibited higher MRI relaxivity than Chi-TPP-IOCO (308 and 150 mM^{-1} s^{-1}, respectively), indicating that Chi-IOCO was more effective than Chit-TPP-IOCO as an MRI contrast agent in macrophages. Taken together, Chit-IOCO nanococktail demonstrates outstanding potential for treatment and diagnosis of ROS-related diseases. Potentially, this nanococktail can be easily modified to include new modules, allowing future application of personalized medicine.

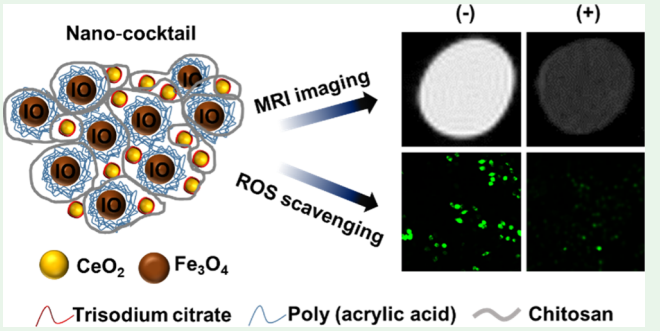

KEYWORDS: *theranostics, nanoparticles, anti-ROS, magnetic resonance imaging (MRI), cerium oxide, iron oxide*

1. INTRODUCTION

Reactive oxygen species (ROS) are ubiquitous in animals as they are products of aerobic metabolism.[1] There are two unpaired electrons on the outer periphery of the oxygen atom. Different ROS can be generated by increasing the electrons around the oxygen.[2] Common examples include hydrogen peroxide (H_2O_2), superoxide anion ($^{\bullet}O_2^-$), peroxide ($^{\bullet}O_2^{-2}$), and hydroxyl radical ($^{\bullet}OH$).[3] It has been established that excessive levels of ROS can damage cells and gene structures which lead to the development of many diseases.[4,5] Inflammatory diseases such as atherosclerosis[6−8] and rheumatoid arthritis[9] are very typical type of ROS-related diseases.[10] ROS can be produced by active macrophages and are enriched in plaques in atherosclerosis.[11] As the disease progresses, ROS can accelerate the growth and instability of plaques.[12] Eventually, the plaques rupture and form the thrombus, leading to fatal diseases such as stroke and ischemic heart diseases.[13,14] In rheumatoid arthritis, ROS such as hydrogen peroxide are mainly produced by chondrocyte cells. These ROS can destroy proteins, DNA, and lipids in joints which ultimately leads to the damage of the cartilage.[9,15] Therefore, the regulation of ROS is a promising approach of treatment in inflammation-related diseases.

In the past few decades, hundreds of anti-ROS compounds have been discovered.[16,17] Antioxidants cannot persistently scavenge ROS after reacting with the oxygen free radicals. Therefore, larger doses or multiple injections of antioxidants

Received: January 15, 2021
Accepted: March 18, 2021

https://doi.org/10.1021/acsanm.1c00141
ACS Appl. Nano Mater. XXXX, XXX, XXX−XXX

Scheme 1. Image Illustrating the Synthesis of Chit-IOCO and Chit-TPP-IOCO[a]

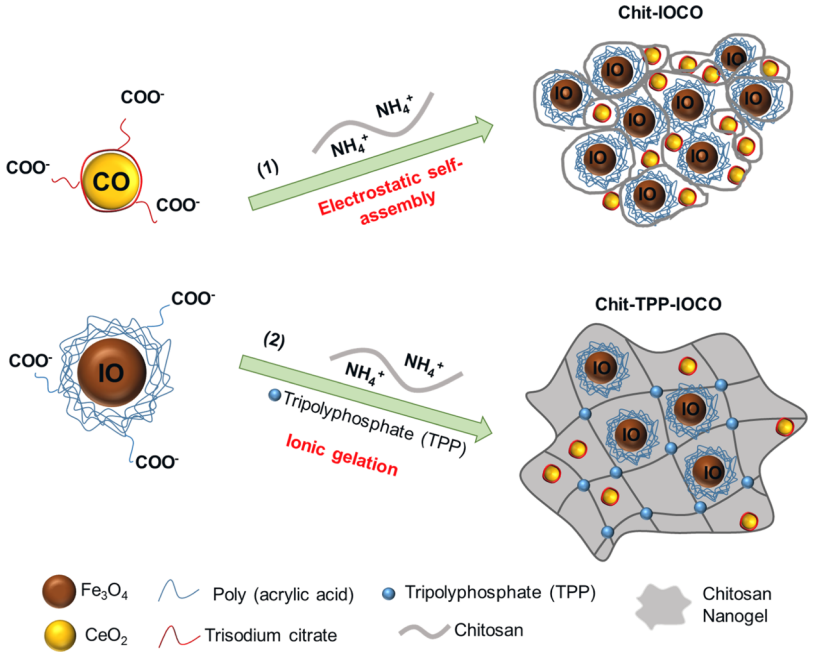

[a](1) Chit-IOCO nanoparticles were prepared via the electrostatic self-assembly method between the positively charged chitosan and the negatively charged IO-PAA and CO-TSC. CO-TSC was first dialyzed against 1 L of Milli-Q water for 30 min. Then, a mixture solution (0.5 mL) of IO-PAA and CO-TSC was pumped (0.2 mL/min) into 4.5 mL of filtered (0.45 μm) chitosan (pH 4.8) to form the chitosan-IOCO nanoparticles. (2) Chit-TPP-IOCO nanoparticles were prepared via the ionic gelation method between chitosan and TPP (a cross-linking reagent), which encapsulates IO-PAA and CO-TSC within its nanogel structure. CO-TSC was first dialyzed against 1 L of Milli-Q water for 30 min. After that, a mixture solution (2.5 mL) of IO-PAA (0.15 mg), CO-TSC (0.15 mg), and TPP (3.15 mg) was pumped (0.2 mL/min) in 5 mL of 0.1% (w/w) filtered (0.45 μm) chitosan (pH 4.8) with continuous stirring for 1 h to form the chitosan-TPP-IOCO nanoparticles.

are required to treat chronic inflammatory diseases.[18] Recently, the anti-ROS property of cerium oxide has been investigated and confirmed by several studies.[19,20] Cerium oxide nanoparticles are unique due to its convertible surface valence unlike other antioxidants. Both trivalent cerium atoms (Ce^{3+}) and tetravalent cerium atoms (Ce^{4+}) are on the surface of cerium oxide.[21] Ce^{3+} on the surface works as an analogue of superoxide dismutase. It can transform superoxide radicals into oxygen and hydrogen peroxide ($Ce^{3+} + O_2^{-\bullet} + 2H^+ \rightarrow Ce^{4+} + H_2O_2$). Ce^{4+} produced by this reaction can scavenge hydrogen peroxide and generate hydrogen ions and water, eventually eliminating ROS. Due to the absorption of hydrogen electrons, Ce^{4+} is then converted into original Ce^{3+} ($Ce^{4+} + H_2O_2 \rightarrow Ce^{3+} + H^+ + H_2O$).[22] Hence, this irreplaceable anti-ROS property allows cerium oxide to be utilized as a potential ROS scavenger for ROS-related diseases.[23,24]

Modern diagnostic approaches for ROS-related diseases are indispensable in current research and treatment.[25] Superparamagnetic iron oxide nanoparticles (SPIONs) have been widely employed as contrast agents for molecular magnetic resonance imaging (MRI).[26,27] SPIONs have lower biological toxicity and stronger proton relaxation than conventional paramagnetic gadolinium MRI contrast agents.[28] Multiple SPION-based nanomaterials have been developed for imaging and detection of ROS-related or inflammatory diseases,[29,30] cardiovascular diseases,[29,31−42] and cancerous diseases.[43,44]

In this study, we investigated the feasibility to develop chitosan nanococktails containing both nanoceria and iron oxide nanoparticles for ROS-related theranostics. Such nanosystems are expected to provide both therapeutic effect (scavenging ROS) and diagnostic capability (detecting ROS-overexpressed areas or disease sites). The combination of therapeutic agents with imaging materials also allows tracking of the therapeutics and their biodistribution. Here, we synthesized poly(acrylic acid)-coated iron oxide (IO-PAA) nanoparticles and trisodium citrate coated cerium oxide (CO-TSC) nanoparticles as our functional modules. We then utilized chitosan, a natural biopolymer extracted from the shells of marine organisms,[45] as a nontoxic carrier of both IO-PAA and CO-TSC to prepare theranostic nanomaterials. Theranostic chitosan nanoparticles (Chit) containing IO-PAA and CO-TSC were prepared by two different approaches: (1) self-assembly between the positively charged chitosan and the negatively charged IO-PAA and CO-TSC nanoparticles and (2) ionic gelation between chitosan and tripolyphosphate (TPP), a cross-linker (Scheme 1). The resulting Chit-IOCO and Chit-TPP-IOCO nanoparticles were characterized *in vitro* to assess their cytotoxicity, anti-ROS, and MRI contrast capabilities.

2. METHODS

2.1. Materials. All chemicals were reagent grade and utilized without further purification unless specified. Iron(II) ammonium sulphate, hydrochloric acid (reagent grade, 37%), ammonium hydroxide solution (30% NH_4OH in H_2O), cerium nitrate hexahydrate, ammonium cerium nitrate, sodium acetate trihydrate, acetic acid, low-molecular-weight chitosan, TPP, hydrogen peroxide, 2,2′-azino-bis(3-ethylbenzothiazoline-6-sulphonic acid) (ABTS), horseradish peroxidase (HRP), 2′,7′-dichlorodihydrofluorescein diacetate (DCF-DA), sodium dodecyl sulfate, and lipopolysaccharide (LPS) were purchased from Sigma-Aldrich. Bovine serum albumin was purchased from Bovogen Biologicals Pty Ltd. Trisodium citrate (TSC) was purchased from Chem-supply. Hydrogen peroxide

https://doi.org/10.1021/acsanm.1c00141
ACS Appl. Nano Mater. XXXX, XXX, XXX−XXX

(H_2O_2) was purchased from EMSURE Merck. Water used in all experiments is Milli-Q water. Phosphate-buffered saline (PBS), RPMI 1640 medium, fetal bovine serum, penicillin−streptomycin solution, L-glutamine, and PrestoBlue cell viability reagent were purchased from Thermo Fisher Scientific.

2.2. Synthesis of Iron Oxide Nanoparticles. The IO-PAA nanoparticles were prepared by the coprecipitation method.[30] Briefly, 200 mg of PAA was dissolved in 50 mL of Milli-Q water. The PAA solution was purged with nitrogen for 30 min and then heated at 130 °C to reflux using an oil bath. A mixture of 0.51 mM $FeCl_3{\cdot}6H_2O$ (0.1378 g) and 0.25 mM $(NH_4)_2Fe(SO_4)_2{\cdot}6H_2O$ (0.099 g) was dissolved in 1 mL of 37% concentrated HCl. The mixed solution was then quickly added into the hot PAA solution. After stirring for 5 min, 15 mL of 30% concentrated ammonia solution was added into the mixture, followed by refluxing the solution for 2 h. The resulting solution was concentrated using a 50k molecular weight cutoff Amicon filter (Millipore, Inc.). The concentrated solution was then dialyzed against 5 L of water at pH 10 for 1 day and pH 7 for 3 days. The PAA-coated iron oxide nanoparticles were collected and stored at 4 °C.

2.3. Synthesis of Cerium Oxide Nanoparticles. Cerium oxide nanoparticles were prepared by the coprecipitation method. $(NH_4)_2Ce(NO_3)_6$ (0.685 g) and CH_3COONa (2.5 g) were dissolved in deionized water (17.5 mL), and then, CH_3COOH (2.5 mL) was added to the solution. After stirring at room temperature for 1 h, the mixture was heated at 100 °C in an oil bath with condensation reflux for 2 h. Finally, yellow precipitates were separated by centrifugation (6000*g*) for 10 min, washed twice with deionized water, and then resuspended in 5 mL of H_2O.

The TSC-coated cerium oxide nanoparticles (CO-TSC) were then prepared by mixing 100 mg of cerium oxide nanoparticles with 0.1 M TSC in 15 mL of H_2O for 24 h. The stirred mixture was then filtered by a 100k molecular weight cutoff Amicon filter (Millipore, Inc.) at 10,000*g* for 1 min to remove the large agglomerates. The CO-TSC nanoparticles were stored in 0.1 M TSC solution before use. The nanoparticle solution was dialyzed against water using 10k MWCO SnakeSkin tube before further use and tests.

2.4. Synthesis of Chi-IOCO. Chit-IOCO nanoparticles were prepared *via* the ionic gelation method using IO-PAA and CO-TSC as the cross-linking reagents. CO-TSC was first dialyzed against 1 L of Milli-Q water for 30 min. Then, a mixture solution (0.5 mL) of IO-PAA and CO-TSC was pumped (0.2 mL/min) into 4.5 mL of filtered (0.45 μm) chitosan (pH 4.8) to form the chitosan-IOCO nanoparticles. Different concentrations of chitosan, IO-PAA, and CO-TSC with different pumping speeds and incubation times were used to optimize the nanocomposite. The mixture was then centrifuged at 10,000*g* for 30 min followed by sonication for total 5 min (cooling down on ice every 30 s of the sonication, 50% amplitude). Iron and cerium concentrations were measured by inductively coupled plasma optical emission spectrometry (ICP−OES).

2.5. Synthesis of Chit-TPP Nanoparticles. Chit-TPP nanoparticles were prepared *via* the ionic gelation method using TPP as the cross-linking reagent. Briefly, TPP (2.5 mL) was pumped (0.2 mL/min) into 5 mL of 0.1% (w/w) filtered (0.45 μm) chitosan (pH 4.8) to form the chit-TPP nanoparticles. Different concentrations of TPP and incubation times were used to optimize the nanoparticles. The mixture was then centrifuged at 10,000*g* for 30 min followed by sonication for total 5 min (cooling down on ice every 30 s of the sonication, 50% amplitude).

2.6. Synthesis of Chit-TPP-IOCO Nanoparticles. Chit-TPP-IOCO nanoparticles were prepared *via* the ionic gelation method using IO-PAA, CO-TSC, and TPP as the cross-linking reagents. CO-TSC was first dialyzed against 1 L of Milli-Q water for 30 min. After that, a mixture solution (2.5 mL) of IO-PAA (0.15 mg), CO-TSC (0.15 mg), and TPP (3.15 mg) was pumped (0.2 mL/min) in 5 mL of 0.1%(w/w) filtered (0.45 μm) chitosan (pH 4.8) with continuous stirring for 1 h. The stirred mixture was then centrifuged at 10,000*g* for 30 min followed by sonication for total 5 min (cooling down on ice every 30 s of the sonication, 50% amplitude). Iron and cerium concentrations were measured by ICP−OES.

2.7. Characterization of Nanoparticles. Transmission electron microscopy (TEM) images were collected on a JEOL-JEM-1010 transmission electron microscope operating at an accelerating voltage of 120 kV. The samples on the copper grid were stained with phosphotungstic acid (10 mg/mL, pH adjusted to 7.3 by sodium hydroxide) for 30 s to visualize chitosan, and the remaining acid solution was removed gently by a piece of tissue. The hydrodynamic size, size distribution, and zeta potential (ZP) of the nanoparticles were measured using a Zetasizer Nano ZS (Malvern) analyzer. Fourier transform infrared spectroscopy (FTIR) spectra were collected using a Nicolet 5700 FT-IR spectrometer. The surface composition of the cerium oxide nanoparticles was analyzed by X-ray photoelectron spectroscopy (XPS) using a Kratos Axis Ultra photoelectron spectrometer.

2.8. Anti-H_2O_2 Capability of Nanoparticles. Nanoparticles of different concentrations ([Ce]: 0, 20, 40, 60, 80, and 100 μg/mL; [Fe]: 18.2, 36.4, 54.6, 72.8, and 91.0 μg/mL; [chitosan]: 828.6, 1657.1, 2485.7, 3314.3, and 4142.9 μg/mL) were treated with 0.1 mM H_2O_2 in a 96-well plate for 1 h at 37 °C with shaking at 200 rpm. 0.01 unit of HRP was added into each reaction followed by 10 min incubation at RT. 8.7 mM of ABTS was then added into the reaction, and the absorbance of samples at 405 nm was measured by an EnSight Multimode Plate Reader (PerkinElmer) microplate reader. The absorbance of 0 μg/mL sample was determined as 0% ROS scavenging.

2.9. MRI. The T_2 relaxation time and MRI of the nanoparticles (Fe: 0.03, 0.06, 0.12, 0.25, and 0.5 mM) were acquired using a Bruker 9.4 T MRI scanner running Paravision 6.0.1. T_2-weighted relaxivity (r_2) is generally defined as the slope of the linear regression generated from a plot of the measured relaxation rate ($1/T_2$) versus the concentration of the contrast agent (iron, Fe). T_2 values were calculated using a 2D multislice multi echo spin echo sequence using TR = 2630 ms, 32 echoes (5−160 ms), 0.117 × 0.117 mm in-plane resolution. The acquisition time was 11 min.

2.10. Cell Culture. Macrophage J774A.1 cells were attained from the American Type Culture Collection. The cells were maintained in a nontreated 100 × 20 mm cell culture dish containing RPMI 1640 with fetal calf serum (10%), penicillin (100 U/mL), and L-glutamine (1%) and cultured in an incubator at 37 °C with 5% CO_2.

2.11. Biocompatibility of the Nanoparticles—Cytotoxicity Study. Macrophages were detached by 2 mL of cold 1× PBS when the cell confluence reached approximately 85%. Then, the cells were seeded into a 96-well plate at a density of 10,000 cells/well. After 24 h of incubation, the cells were treated with different concentrations of cerium in different nanoparticles Chit-IOCO, Chit-TPP, and Chit-TPP-IOCO (Ce: 0, 0.1, 0.5, 1.0, 5.0, 10.0, and 20.0 μg/mL). After 24 h nanoparticle treatment, the cells were treated with 1× PrestoBlue cell viability reagent for 30 min to detect viability and proliferation of macrophage cells by fluorescence intensity. The fluorescence intensity was measured by an EnSight Multimode Plate Reader (PerkinElmer) with an excitation wavelength of 560 nm and an emission wavelength of 590 nm. The fluorescence of the 0 mg/mL sample was determined as 100% viability of the macrophages.

2.12. *In Vitro* ROS Scavenging Cell-Based Assay. Macrophage J774A.1 cells were seeded into a 96-well plate at a density of 10,000 cells/well. After 24 h of incubation, the cells were separately treated with 1 μg/mL LPS along with different nanoparticles in different concentrations of cerium (0, 0.1, 0.5, 1.0, 5.0, and 10.0 μg/mL). After an additional 24 h of incubation, macrophages were treated with DCF-DA (25 μM) for 10 min in the incubator at 37 °C and 5% CO_2. The fluorescence intensity was measured by an EnSight Multimode Plate Reader (PerkinElmer) (ex/em: 485/535 nm), and fluorescence images were taken by a Nikon ECLIPSE Ti microscopy system with a Photometrics CoolSNAP HQ2 camera and a Nikon INTENSILIGHT C-HGFIE fluorescent light source.

2.13. *In Vitro* Cell MRI. Macrophages J774A.1 were seeded into a 6-well plate at a density of 300,000 cells/well. After 24 h of incubation, the cells were treated with Chit-IOCO or Chit-TPP-IOCO with 5 and 10.0 μg/mL concentrations of cerium for 24 h. Subsequently, the cells were washed with PBS three times. The cells

https://doi.org/10.1021/acsanm.1c00141
ACS Appl. Nano Mater. XXXX, XXX, XXX−XXX

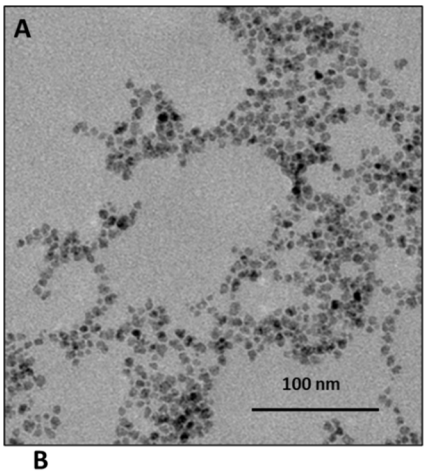

B

Z-average (nm)	15.0 ± 0.5
PDI	0.22 ± 0.01
Number (nm)	7.1 ± 1.8
Zeta potential (mV)	-29.2 ± 1.9

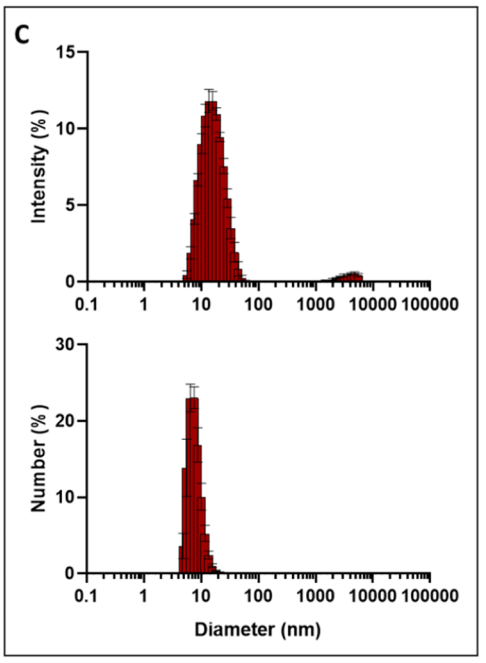

Figure 1. Characteristics of IO-PAA. (A) TEM images of IO-PAA (scale bar: 100 nm). (B) Nanoparticle size and ZP measured by Zetasizer ZS. ZP data showed that IO-PAA nanoparticles are negatively charged. (C) DLS size distribution of the IO nanoparticles.

were then detached and centrifuged at 200 g for 5 min. The cells were subsequently resuspended with 200 μL of warm 1% low-gelling temperature agarose, and 50 μL was quickly transferred into the prepared phantom vessel (Scheme S1). The T_2 relaxation time was measured using the same parameters described above (Section 2.9).

2.14. Statistical Analysis of Data. Data are presented as mean standard deviation. One-way ANOVA was used in the analysis of significant difference. A p value of <0.05 was considered significant. Graphs were plotted using GraphPad Prism 8.

3. RESULTS AND DISCUSSION

3.1. Characterization of Iron Oxide Nanoparticles. SPIONs have been employed as MRI contrast agents in several studies. SPIONs can provide a stronger MRI signal and have lower toxicity than the gadolinium-based contrast agents.[46,47] In this study, the IO-PAA nanoparticles were successfully synthesized using a coprecipitation method. The TEM images (Figure 1A) showed that the IO-PAA nanoparticles are around 5−8 nm in diameter. The hydrodynamic size of IO-PAA was around 15 nm with a polydispersity index (PDI) of 0.22. The surface ZP of the IO-PAA particles was negative (−29.21 mV) due to the PAA coating layer (Figure 1B). This property is beneficial for the following synthesis of the theranostic chitosan-based material. Dynamic light scattering (DLS) plots (Figure 1C) show the size distribution of IO-PAA.

3.2. Characterization and Optimization of Cerium Oxide Nanoparticles. Cerium oxide nanoparticles were synthesized using $(NH_4)_2Ce(NO_3)_6$ and CH_3COOH.[48] Cerium oxide nanoparticles were then coated with TSC, resulting in negatively charged cerium oxide nanoparticles (CO-TSC) which were used as the therapeutic module in the following theranostic chitosan-based nanocomposite. Figure 2A(i) shows that CO-TSC have a homogeneous size of 3 nm. Figure 2A(ii) shows the size distribution of CO-TSC. Figure 2A(iii) indicates that CO-TSC had an average hydrodynamic size of around 5 nm with a low PDI of 0.15. Figure 2A(iii) also confirms that CO-TSC were negatively charged. However, it was observed that CO-TSC was not stable in water solution as some aggregation formed after 24 h (Figure S1). CO-TSC nanoparticles were stable in TSC solution and showed no significant change in particle size and surface charge (Figure 2B). Therefore, CO-TSC were stored in TSC solution to keep their size and ZP stable before further use.

XPS was employed to determine the different oxidation states of cerium which is related to the anti-ROS bioactivity of cerium oxide nanoparticles.[49] As shown in Figure 2C, only tetravalent cerium (Ce^{4+}) oxidation states are present in cerium oxide nanoparticles. After coating with reductive TSC, both trivalent cerium (Ce^{3+}) and tetravalent cerium (Ce^{4+}) oxidation states were detected on the surface of CO-TSC nanoparticles (20% of Ce^{3+}). Previous studies demonstrated that cerium oxide nanoparticles with around 20% of surface Ce^{3+} had anti-ROS activity.[22] Therefore, it is expected that the synthesized CO-TSC with 20% of Ce^{3+} could be a potential anti-ROS module that can be loaded into chitosan nanoparticles. Its anti-ROS capability was investigated and described in the following sections.

3.3. Optimization of the Nanococktail Synthesis. *3.3.1. Chit-IOCO.* The newly synthesized Chit-IOCO nanoparticles were prepared by mixing the negatively charged IO-PAA and CO-TSC with positively charged chitosan in solution. The concentrations and ratios were optimized to obtain theranostic chitosan nanomaterials with good size, ZP, and high loading of CO-TSC and IO-PAA. In addition, the reaction time, loading speed, and concentration of chitosan solution were also varied to optimize the materials. It is ideal to have Chit-IOCO nanoparticles with size around 100 nm and ZP higher than 20 mV for greater cell uptake in the *in vitro* and *in vivo* studies. The TEM images (Figure 3A(i)) showed that the final Chit-IOCO nanoparticles are around 100 nm in diameter. Nanoclusters of IO-PAA and CO-TSC are seen in the image. It is therefore suggested that the formation of Chit-IOCO is via the self-assembly of the positively charged chitosan and the negatively charged IO-PAA and CO-TSC and that there is no gelation formation. The hydrodynamic size of

https://doi.org/10.1021/acsanm.1c00141
ACS Appl. Nano Mater. XXXX, XXX, XXX−XXX

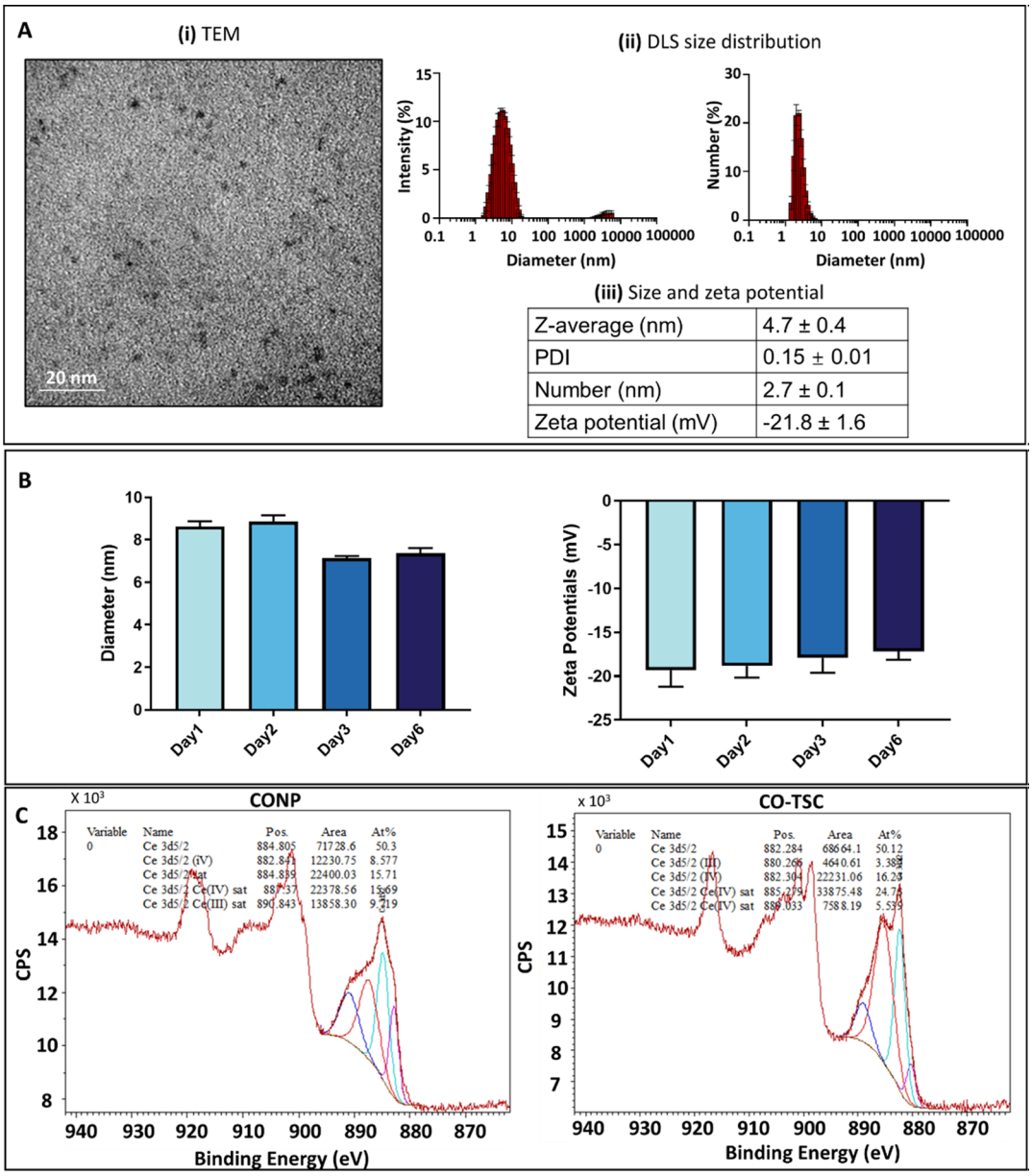

Figure 2. Characteristics of CO-TSC. (A) Size and ZP of CO-TSC. (i) TEM image of CO-TSC, (ii) DLS size distribution of CO-TSC, and (iii) ZP and PDI of CO-TSC. (B) Stability studies of CO-TSC in TSC solution. Size and ZPs of the CO-TSC nanoparticles were measured in TSC solution at days 1, 2, 3, and 6. (C) XPS of cerium oxide nanoparticles. The Ce^{3+}/Ce^{4+} ratio is an important characteristic that is related to the antioxidant activity of the cerium oxide nanoparticles. The graph shows the Ce scans of cerium oxide nanoparticles. The XPS result indicated that there is no Ce^{3+} in cerium oxide nanoparticles but 20% of Ce^{3+} in CO-TSC.

Chit-IOCO was around 150 nm with a low PDI of 0.13 (Figure 3A(iii)). DLS size intensity plots (Figure 3A(ii)) demonstrated that the optimized IO-PAA has a narrow size distribution. Figure 3B(i) shows that the size of Chit-IOCO nanoparticles was less affected by the loading speed of the IO-PAA and CO-TSC mixed solution. Thus, a pumping speed at 0.2 mL/min was employed in further optimization steps. Figure 3B(ii) depicts that the size of the final Chit-IOCO nanoparticles increases as the stirring time of the mixture increases. A 1 h stirring time was optimal and chosen for all subsequent syntheses to control the size of the nanoparticles at around 100 nm. In addition, higher chitosan solution concentrations increased the size of Chit-IOCO nanoparticles. The higher surface charge may be due to larger amounts of chitosan involved in the formation of nanoparticles. 0.8 mg/mL concentration of the chitosan was chosen to be used in the later synthesis for smaller particle size and higher ZP (Figure 3B(iii),(iv)). The concentration of IO-PAA and CO-TSC used in the synthesis of Chit-IOCO was another critical condition for the final size of Chit-IOCO. Figure 3B(iv) shows that the particle size of Chit-IOCO was proportional to the concentration of IO and CO-TSC; hence, the particle size could be controlled by increasing or decreasing the concentration of IO and CO-TSC. Concentrations of 0.06 mg/mL of IO and 0.06 mg/mL of CO-TSC were chosen for further studies. Overall, it was demonstrated that the size of Chit-IOCO nanoparticles was greatly affected by the reaction time, chitosan concentration, and concentration of IO CO-TSC, while it was less affected by the pumping speed.

https://doi.org/10.1021/acsanm.1c00141
ACS Appl. Nano Mater. XXXX, XXX, XXX−XXX

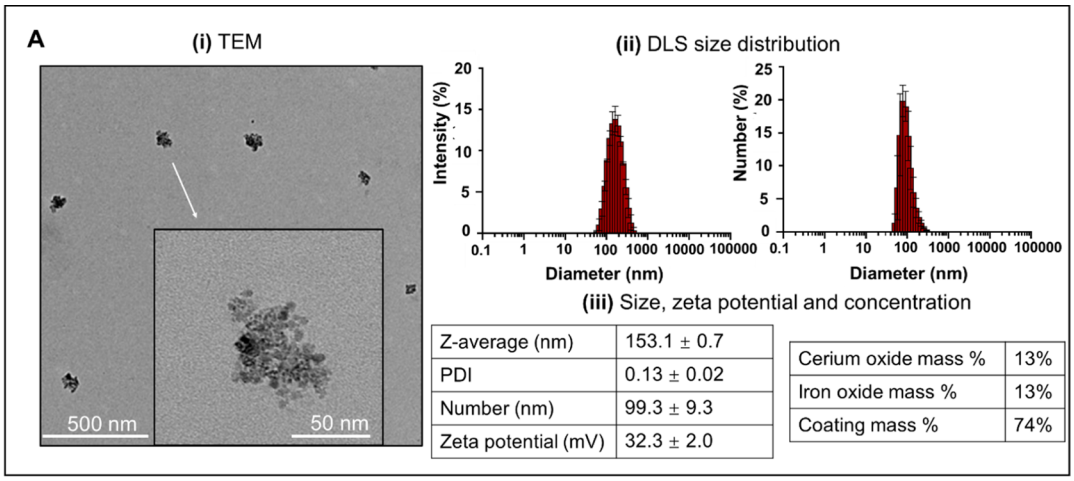

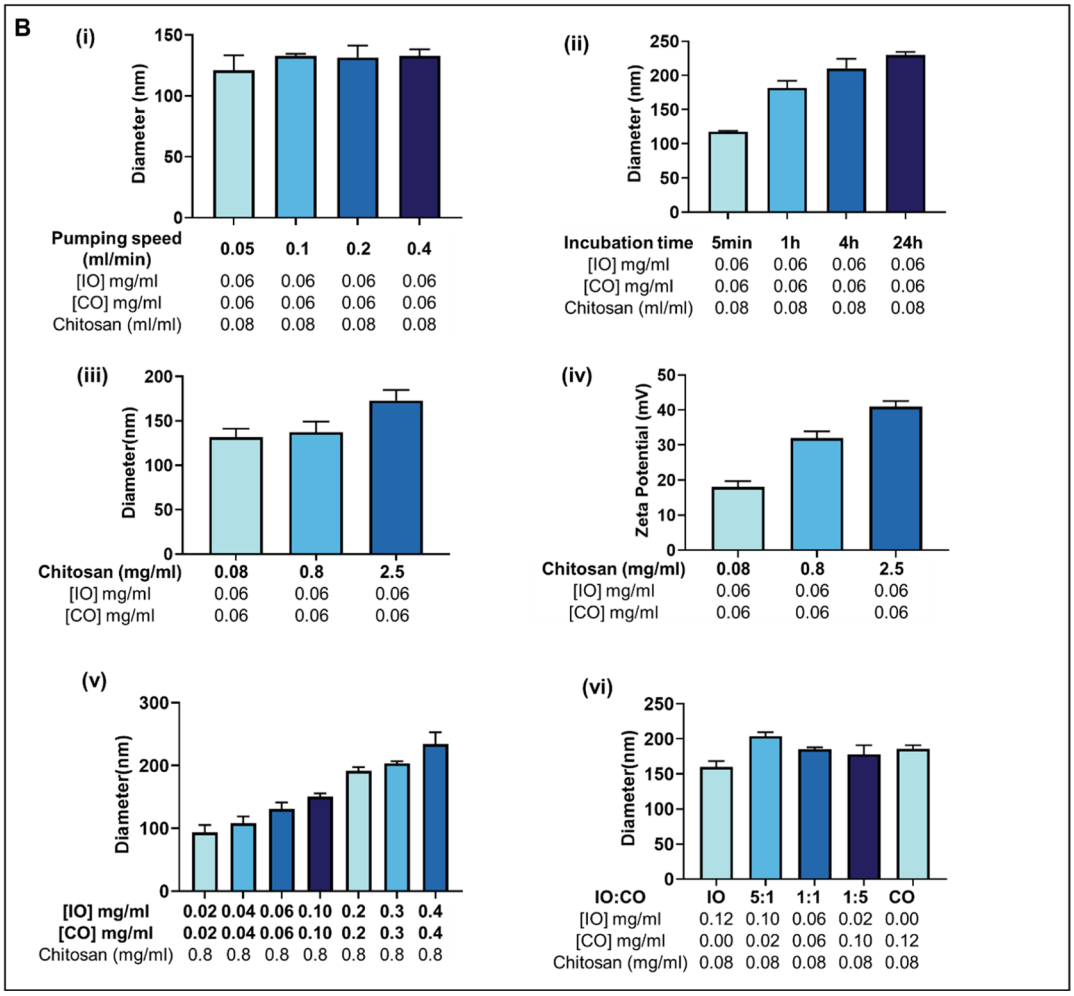

Figure 3. Characteristics and optimization of IO-PAA and CO-TSC loaded chitosan nanoparticles (Chit-IOCO). (A) Characteristics of IO-PAA and CO-TSC loaded chitosan nanoparticles (Chit-IOCO). (i) TEM image of Chit-IOCO, (ii) DLS size distribution of Chit-IOCO, (iii) ZP, PDI, and mass percentage of components. (B) Optimization of Chit-IOCO. (i) Size of the Chit-IOCO nanoparticles after synthesis with different pumping speeds of IO-PAA and CO-TSC mixture into chitosan solution. (ii) Size of the Chit-IOCO nanoparticles after synthesis with different incubation times. (iii) Size of the Chit-IOCO nanoparticles after synthesis with different chitosan concentrations. (iv) ZP of the Chit-IOCO nanoparticles after synthesis with different chitosan concentrations. (v) Size of the Chit-IOCO nanoparticles after synthesis with different concentrations of IO-PAA and CO-TSC. (vi) Size of the Chit-TPP nanoparticles after synthesis with different IO-PAA/CO-TSC ratios.

We also tested the effect of the ratio of IO-PAA and CO-TSC (IO/CO) on the synthesis. The results of DLS (Figure 3B(v)) suggested that different IO/CO ratios did not influence the size of Chit-IOCO nanoparticles. Thereafter, IO/CO at 1:1 was chosen to equally include both imaging and treatment agents in the theranostic materials. Overall, the Chit-IOCO nanococktails were successfully synthesized *via* the electrostatic self-assembly method. Since Chit-IOCO can be easily adjusted

https://doi.org/10.1021/acsanm.1c00141
ACS Appl. Nano Mater. XXXX, XXX, XXX−XXX

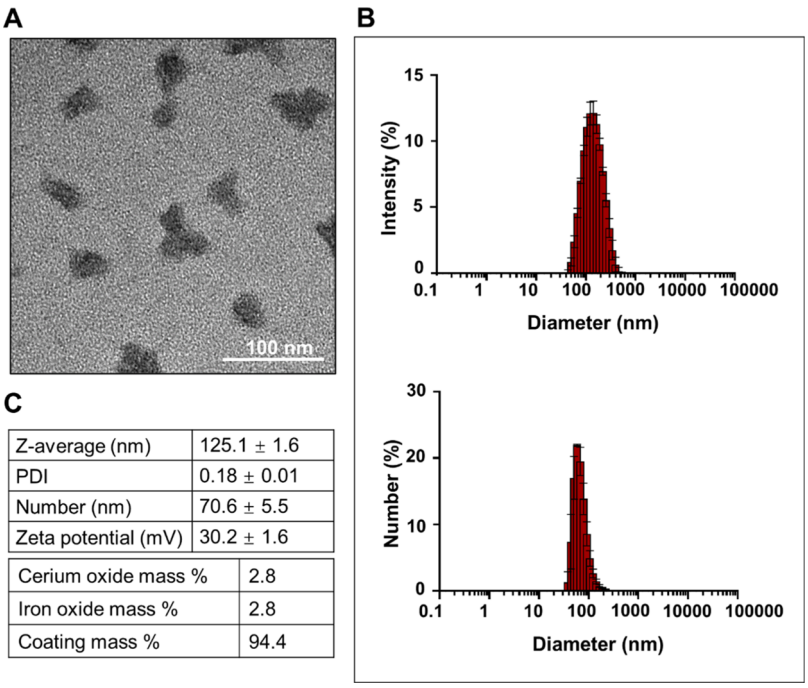

Z-average (nm)	125.1 ± 1.6
PDI	0.18 ± 0.01
Number (nm)	70.6 ± 5.5
Zeta potential (mV)	30.2 ± 1.6

Cerium oxide mass %	2.8
Iron oxide mass %	2.8
Coating mass %	94.4

Figure 4. Characteristics of Chit-TPP-IOCO. (A) TEM images of Chit-TPP-IOCO nanoparticles (scale bar, 100 nm). (B) DLS size distribution of the Chit-TPP-IOCO nanoparticles. (C) Nanoparticle size and ZP measured by DLS Zetasizer and mass percentage of components.

with different IO/CO ratios if required, it is feasible to manipulate the materials for different purposes. It is possible to use a single module to synthesize chitosan nanoparticles for only one purpose. Similarly, another module can be added into the system to enhance treatment or imaging capabilities. For example, we can add TSC-coated gold nanoparticles as a module for thermodynamic therapy.[50]

3.3.2. Chit-TPP. Chit-TPP nanoparticles were prepared by mixing the negatively charged TPP with positively charged chitosan solution.[51] As shown in Figure S2A, the Chit-TPP nanoparticles were positively charged with the hydrodynamic size of around 110 nm with a PDI of 0.23. Figure S2B shows the size distribution of the optimized Chit-TPP nanoparticles. Here, the effects of TPP concentration and reaction time on the Chit-TPP nanomaterial size were investigated. Figure S2C,D shows that both the concentration of TPP and reaction time had no significant effects on the size of Chit-TPP nanoparticles. Therefore, the TPP concentration of 0.42 mg/mL and 1 h stirring were selected as the ideal parameters in the synthesis of Chit-TPP and later Chit-TPP-IOCO. Chit-TPP nanoparticles were used as a non-cerium control for the Chit-TPP-IOCO nanoparticles in viability studies.

3.3.3. Chit-TPP-IOCO. As TPP is a widely used cross linker for chitosan nanoparticles,[52] here, we attempted to employ TPP as a cross linker to prepare Chi-TPP-IOCO with the aim to investigate whether TPP could improve the formation of the nanococktails. Based on previous exploration of the synthesis conditions, the mixture solution containing TPP (0.42 mg/mL), IO-PAA (0.06 mg/mL), and CO-TSC (0.06 mg/mL) was pumped (0.2 mL/min) into chitosan solution (0.67 mg/mL) and then stirred for 1 h to synthesize Chit-TPP-IOCO nanoparticles. TEM image shows that Chit-TPP-IOCO nanoparticles were approximately 60 nm in size (Figure 4A). Interestingly, opposite to Chit-IOCO, in Chit-TPP-IOCO, clusters of IO and CO nanoparticles cannot be seen in the image, but a solid structure is observed. It is therefore suggested that the formation mechanisms of Chit-IOCO and Chit-TPP-IOCO are different. Chit-IOCO is formed by electrostatic self-assembly, while Chit-TPP-IOCO is formed by ionic gelation, which encapsulates IO-PAA and CO-TSC within its nanogel. It is well-known that chitosan forms hydrogel in the presence of TPP. The hydrodynamic size of Chit-TPP-IOCO nanoparticles was 125 nm with the surface ZP of 30.2 mV (Figure 4B). Figure 4C shows the size distribution of Chi-TPP-IOCO.

FTIR spectrometry was used to corroborate the loading and coating of the above NPs. As shown in Figure S3A, peaks at 2898 cm^{-1} showed C−H bonds, 1705 cm^{-1} indicated C═O bonds, 1400 cm^{-1} showed C−O bonds, 1104 to 1163 cm^{-1} showed C−C bonds, and at 555 cm^{-1} were Fe−O bonds. According to the PAA and iron oxide structure and infrared spectroscopy, PAA was successfully coated on the IO-PAA nanoparticles. For CO-TSC, peaks at 3444−3233 cm^{-1} showed O−H bonds, 1584 cm^{-1} indicated C═O bonds, 1400 cm^{-1} showed C−O bonds, 1064 cm^{-1} and 849 cm^{-1} showed C−C bonds, and at 450 cm^{-1} were Ce−O bonds. The peaks of the chemical bonds (O−H, C−O and C−C) of TSC are present in the FTIR spectra of CO-TSC nanoparticles, indicating that TSC was successfully coated on the nanoparticles (Figure S3B). The next section of the FTIR study was concerned with Chit-TPP. The characteristic bonds[53] at 3259, 2861, 1626, 1536, 1445, 1374, and 1307 cm^{-1} are assigned to O−H bonds, C−H bonds, C═O bonds, N−H bonds, stretching vibration of N−O−P, CH−OH, bonds and CH_2−OH bonds, respectively (Figure S3C). Chit-TPP was formed by electrostatic interaction between the positive amine groups of chitosan and the negative phosphate group of TPP. Thus, N−O−P bonds found in Chit-TPP nanoparticles suggested the successful synthesis of Chit-TPP. For the Chit-TPP-IOCO nanoparticles (Figure S3D), Fe−O bonds, Ce−O bonds, and N−O−P bonds were found in the FTIR spectra, which

https://doi.org/10.1021/acsanm.1c00141
ACS Appl. Nano Mater. XXXX, XXX, XXX−XXX

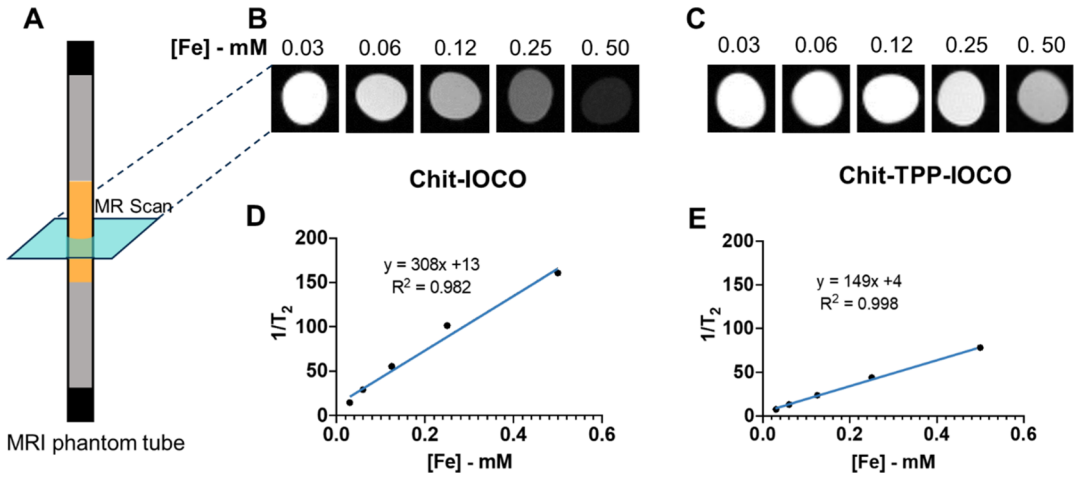

Figure 5. MRI of Chit-IOCO and Chit-TPP-IOCO nanoparticle phantoms. (A) Scheme of MR scan position. (B) MRI images of Chit-IOCO phantoms. Chit-IOCO were diluted to different concentrations of iron followed by imaging using a 9.4 T MRI. (C) MRI images of Chit-TPP-IOCO phantoms. Chit-TPP-IOCO were diluted to different concentrations of iron followed by imaging using a 9.4 T MRI. (D) Relaxation rate plotted against iron concentration of Chit-IOCO. (E) Relaxation rate plotted against iron concentration of Chit-TPP-IOCO.

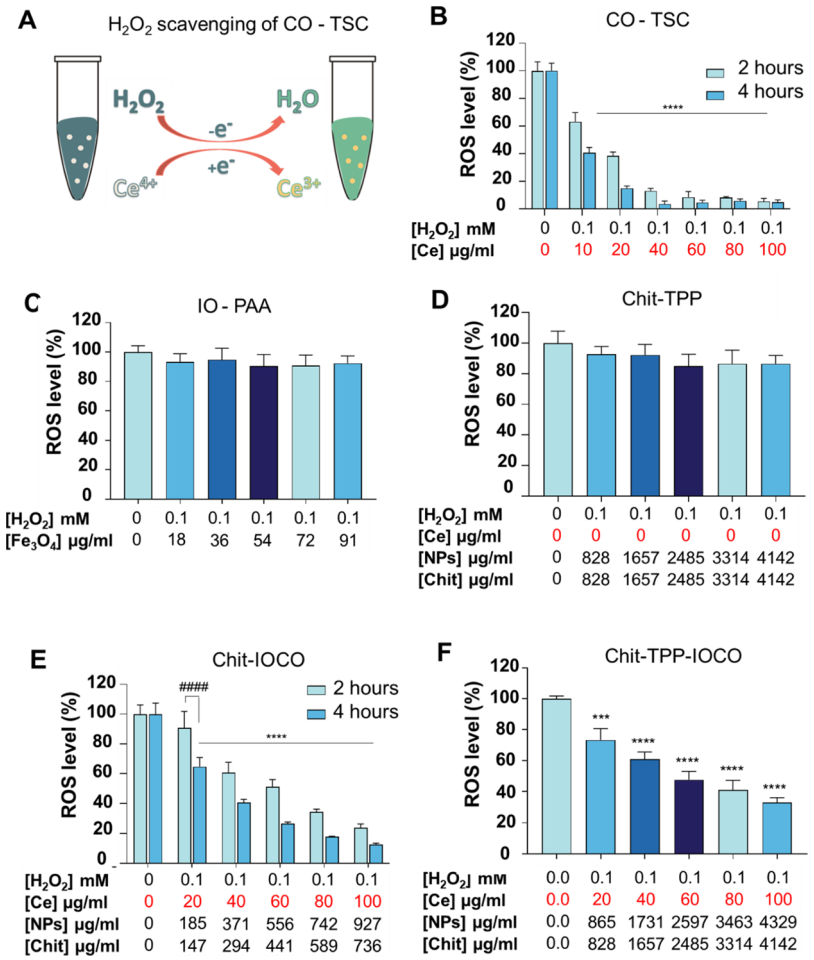

Figure 6. ROS scavenging study of nanoparticles in buffer. (A) Proposed scheme of CO-TSC reaction with H_2O_2. (B) ROS scavenging study of CO-TSC nanoparticles in buffer. (C) ROS scavenging study of IO-PAA nanoparticles in buffer. (D) ROS scavenging study of Chit-TPP nanoparticles in buffer. (E) ROS scavenging study of Chit-IOCO nanoparticles in buffer. (F) ROS scavenging study of Chit-TPP-IOCO nanoparticles in buffer. Different concentrations of the nanoparticles were treated with H_2O_2, followed by HRP treatment. Then, ABTS was added into each reaction, and absorbance was measured by a PerkinElmer plate reader. The absorbance of the 0 μg/mL sample was determined as 0% ROS scavenging. * Compared with [Ce]-0 μg/mL control: *$p < 0.05$, **$p < 0.01$, ***$p < 0.001$, ****$p < 0.0001$. # Compared with [Ce]-0.1 μg/mL 2 h control: #$p < 0.05$, ##$p < 0.01$, ###$p < 0.001$, ####$p < 0.0001$.

https://doi.org/10.1021/acsanm.1c00141
ACS Appl. Nano Mater. XXXX, XXX, XXX−XXX

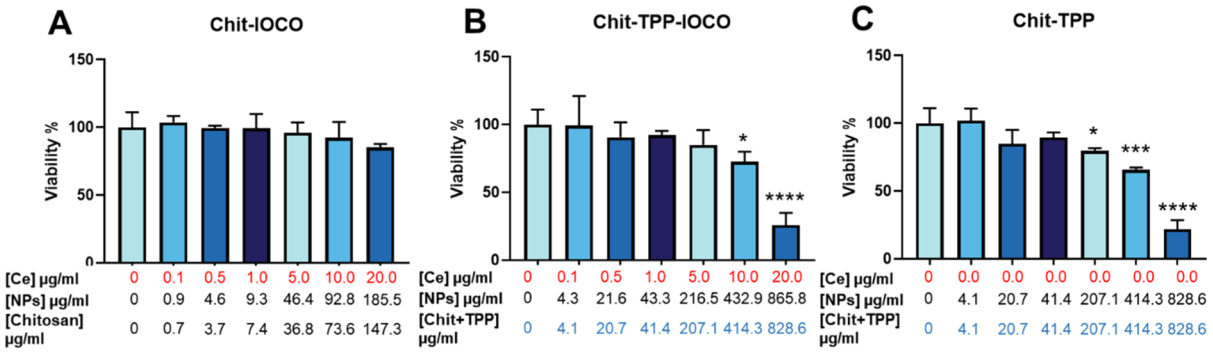

Figure 7. Cytotoxicity study of macrophage cells with Chit-TPP, Chit-IOCO, and Chit-TPP-IOCO nanoparticles. Macrophage cells were incubated with different chitosan nanoparticles for 24 h. Cell viability was detected by the PrestoBlue cell viability kit. The fluorescence intensity was measured by a PerkinElmer plate reader. (A) Viability of the macrophages after 24 h of incubation with Chit-IOCO. (B) Viability of the macrophages after 24 h of incubation with Chit-TPP-IOCO. (C) Viability of the macrophages after 24 h of incubation with Chit-TPP. * Compared with cells only control: *$p < 0.05$, **$p < 0.01$, ***$p < 0.001$, ****$p < 0.0001$.

indicated that IO-PAA and Ce-TSC nanoparticles were successfully loaded in the Chit-TPP-IOCO nanoparticles.

Overall, it was found that the size and ZP of Chit-TPP-IOCO were similar to those of Chit-IOCO nanococktails. Both Chit-IOCO and Chit-TPP-IOCO were synthesized with an irregular shape. Chit-IOCO, however, could load a larger amount of IO-PAA and CO-TSC compared to Chit-TPP-IOCO (Figures 3A(iii) and 4C). The difference in biocompatibility, anti-ROS, and MRI contrast ability of the nanococktails with or without TPP will be investigated in the following studies.

3.4. Chit-IOCO is a Better MRI Contrast Agent than Chit-TPP-IOCO. Chit-IOCO and Chit-TPP-IOCO nanoparticles with different iron concentrations were prepared for MRI phantoms (Figure 5A). The signal intensity of T_2-weighted MR images of both chitosan nanoparticles decreased when the concentration of iron oxide increased. Notably, T_2-weighted MR images (Figure 5B,C) show that Chit-IOCO exhibited stronger T_2 contrast than Chit-TPP-IOCO and may serve as more sensitive T_2 contrast agents. Figure 5D,E shows that Chit-IOCO had a higher transverse relaxivity (r_2) than Chit-TPP-IOCO (308 and 149 mM^{-1}, s^{-1}, respectively). Chit-IOCO showed a steeper slope of relaxation rate than Chit-TPP-IOCO, which could result from the higher iron oxide loading and the lower percentage of chitosan coating content in Chit-IOCO compared to Chit-TPP-IOCO (Figures 3A(iii) and 4C). The difference in the loading of IO-PAA and CO-TSC in Chit-IOCO and Chi-TPP-IOCO could result from the difference in their synthesis methods. In the electrostatic self-assembly method, the positive charged chitosan directly interacted and wrapped around the negative charged IO-PAA and CO-TSC, self-assembling into Chit-IOCO due to electrostatic interactions. In the ionic gelation method, TPP induced the formation of chitosan nanogel and encapsulated IO-PAA and CO-TSC within its structure, forming Chit-TPP-IOCO. Nanogels hold a great amount of water due to the presence of hydrophilic functional groups and limited the number of IO-PAA and CO-TSC that could be encapsulated within their network. The nanogel structure of Chit-TPP-IOCO was also thought to affect its MRI relaxivity as IO-PAA particles were encapsulated within the nanogel structure. On the other hand, due to the self-assembly nature of Chito-IOCO, IO-PAA particles could be positioned within and also on the surface of the nanococktail structure. More Fe^{3+} on the surface of single Chit-IOCO can enhance relaxivity by providing more efficient transfer of magnetization to the surrounding water protons. A previous study showed that transverse relaxivity of iron oxide nanoparticles decreased with increasing coating thickness.[54] The transverse relaxivity (r_2) we obtained with Chit-IOCO is 308 mM^{-1} s^{-1} at 9.4 T, which is comparable to those of clinical iron oxide contrast agents such as Feridex (r_2 = 307 at 9.4 T, r_2 = 93 at 3 T), FeREX (r_2 = 284 at 9.4 T, r_2 = 160 at 3 T), and Resovist (r_2 = 143 at 3 T).[55] Moreover, our nanoparticles are superior than MC03F, an MRI contrast agent in the clinical trial (r_2 = 72 at 9.4 T).[55] Hence, based on these findings, we infer that our nanococktails showed MRI contrast capability similar to commercial MRI agents."

3.5. Chit-IOCO and Chit-TPP-IOCO are Effective ROS Scavengers. We used the H_2O_2−HRP−ABTS system to assess the anti-ROS efficacy of the nanoparticles in the buffer. Briefly, ABTS was oxidized by hydrogen peroxide (H_2O_2) in the presence of HRP as a catalyst. As mentioned previously, ceria can scavenge both H_2O_2 and superoxide radicals when the cerium oxidation state changes between trivalence and tetravalence. Therefore, we incubated our nanoparticles with hydrogen peroxide, followed by the addition of HRP. Finally, ABTS was added to detect ROS (Figure 6A). The result indicated that the percentage of ROS level significantly decreased at higher cerium concentrations and longer incubation time (Figure 6B). The level of ROS decreased sharply from 63 to 9% when the concentration of cerium increased from 10 to 60 μg/mL with 2 h of incubation of the nanoparticles. Subsequently, the level of ROS was maintained approximately 8% when the concentration of cerium was greater than 60 μg/mL. At 4 h of incubation, the level of ROS declined rapidly from 40 to 2% when the cerium concentration was between 10 and 40 μg/mL.

The anti-ROS capabilities of iron oxide and chitosan-TPP nanoparticles were also investigated (Figure 6C,D). No significant anti-ROS effect was observed in both iron oxide and chitosan nanoparticles. However, after the addition of cerium oxide, both nanococktails demonstrated a significant decrease in the ROS level (Figure 6E,F). Figure 6E also demonstrated that incubation with Chit-IOCO for 4 h had a more profound anti-ROS efficacy in comparison to a 2 h incubation for all concentration groups. Comparing Chit-IOCO with Chit-TPP-IOCO at the cerium concentration of 100 μg/mL, Chit-IOCO-treated group showed lower ROS remaining (25%) than the Chit-TPP-IOCO group (35%).

https://doi.org/10.1021/acsanm.1c00141
ACS Appl. Nano Mater. XXXX, XXX, XXX−XXX

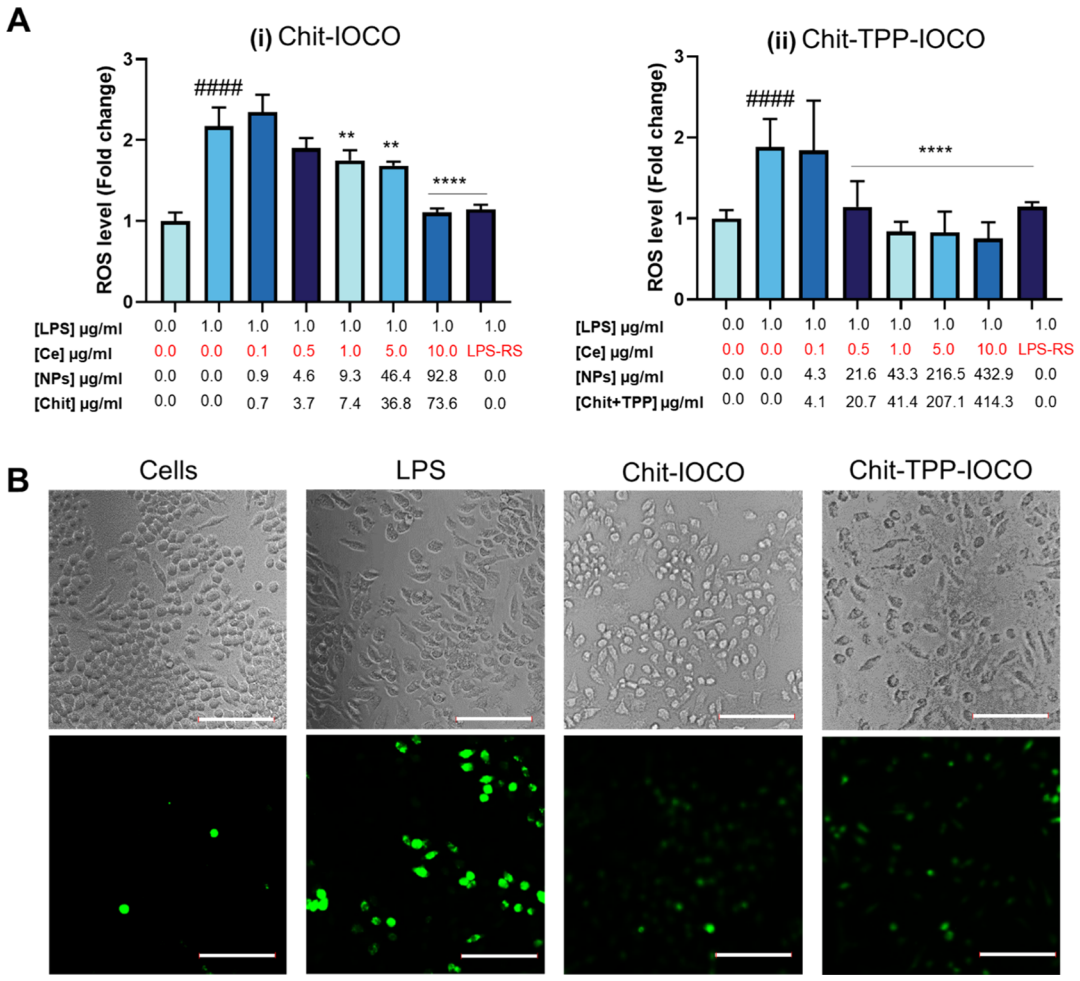

Figure 8. ROS scavenging ability of Chit-IOCO and Chit-TPP-IOCO nanoparticles in macrophage cells. (A) Graphs showing the ROS level of the cells treated with different nanoparticles at different concentrations. (i) Cells treated with Chit-IOCO nanoparticles showed a significant reduction of ROS when the concentration of cerium reached 1 μg/mL. (ii) Chit-TPP-IOCO began to show significant ROS scavenging ability at the cerium concentration of 0.5 μg/mL. (B) Fluorescence images showing the ROS level of the cells treated with or without nanoparticle. Images indicated that both cells treated with Chit-IOCO and Chit-TPP-IOCO nanoparticles exhibited a significantly lower green fluorescence signal than the cells treated with LPS. * Compared with cell only control: $^{*}p < 0.05$, $^{**}p < 0.01$, $^{***}p < 0.001$, $^{****}p < 0.0001$. $^{\#}$ Compared with LPS-stimulated control: $^{\#}p < 0.05$, $^{\#\#}p < 0.01$, $^{\#\#\#}p < 0.001$, $^{\#\#\#\#}p < 0.0001$. Scale bar: 100 μm.

Overall, after loading of the anti-ROS cerium oxide modules, our nanococktails obtained excellent anti-ROS performance. The results also indicated that the loading of CO-TSC into the nanococktails slightly reduced its anti-ROS efficacy, and Chit-IOCO exhibited better performance than Chi-TPP-IOCO.

3.6. Chit-IOCO is More Biocompatible than Chit-TPP-IOCO. The cytotoxicity of the developed nanomaterials was investigated in macrophages. Macrophages were incubated with different concentrations of the nanoparticles for 24 h, followed by PrestoBlue treatment for 30 min. Resazurin inside PrestoBlue was reduced to resorufin in the environment of live cells. Finally, the fluorescence intensity of resorufin was measured by a PerkinElmer plate reader. Notably, Figure 7A demonstrates that Chit-IOCO nanomaterials, at concentrations of cerium from 0.1 to 20 μg/mL, have negligible cytotoxic effects in macrophages. Interestingly, results from Figure 7B indicate that Chit-TPP-IOCO exhibits toxicity in macrophages at a cerium concentration of 10 μg/mL and higher.

Cytotoxicity test was conducted on Chit-TPP nanoparticles with the same concentration of chitosan as Chit-TPP-IOCO to determine if chitosan and TPP are contributing to the toxicity. Here, we did not attempt to test the cytotoxicity of chitosan and TPP alone. It is because chitosan solution or TPP solution alone has physical and chemical properties different from those in the nanoparticle form. Testing the respective cytotoxicity of chitosan and TPP separately in solution will not demonstrate an accurate representation of its true toxicity level in the nanoparticle form. Results from Figure 7C demonstrate that the viability of macrophages decreased to 21% as chitosan and TTP concentrations increased, hence clearly indicating that cytotoxicity is caused by chitosan and TPP. Therefore, ceria did not contribute to the cytotoxicity.

3.7. Theranostics Aspect of Chit-IOCO and Chit-TPP-IOCO—Capabilities to Simultaneously Scavenge ROS and Image Macrophages. Macrophages play a major role in inflammatory and ROS-related diseases.[56] They are cells that produce excessive ROS when the immune system responds to inflammation conditions such as atherosclerosis and rheumatoid arthritis. Toxic ROS can further accelerate the development of the diseases.[56] In our project, we aim to develop a theranostic nanomaterial that can help detect the inflammatory disease site and also suppress the progression of the disease. It can be achieved by targeting macrophages (abundant cells in

https://doi.org/10.1021/acsanm.1c00141
ACS Appl. Nano Mater. XXXX, XXX, XXX−XXX

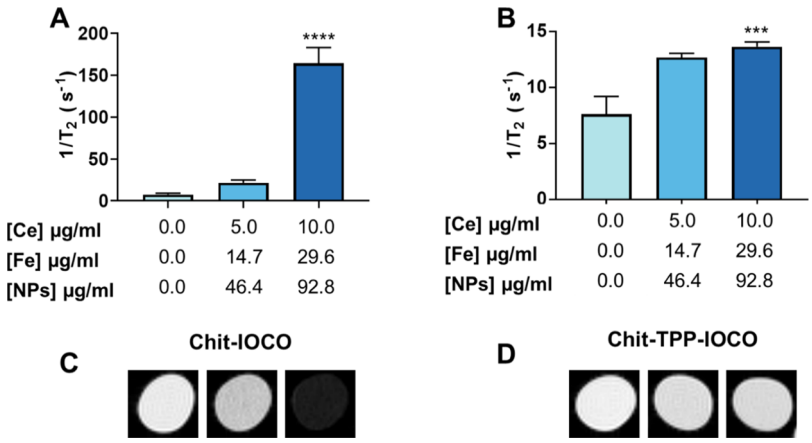

Figure 9. *In vitro* MRI of Chit-IOCO and Chit-TPP-IOCO nanoparticles in macrophage cells. (A) Graph showing the T_2-weighted MRI signal of J774A.1 incubated with or without Chit-IOCO in different concentrations of Fe. (B) Graph showing the T_2-weighted MRI signal of J774A.1 incubated with or without Chit-TPP-IOCO in different concentrations of Fe. (C) T_2-weighted MR images of J774A.1 incubated with Chit-IOCO at different Fe concentrations. (D) T_2-weighted MR images of J774A.1 incubated with Chit-TPP-IOCO at different Fe concentrations. Compared with [Fe] 0 μg/mL: ***$p < 0.001$, ****$p < 0.0001$.

inflammation) and decreasing the ROS level in the macrophages, thus inhibiting subsequent pathology regulation induced by toxic ROS. We have demonstrated that the developed nanococktails are able to image macrophages and scavenge ROS in these cells, potentially suitable for detecting and treating ROS-related diseases.

3.7.1. Macrophage ROS Scavenging Capability. As mentioned above, anti-H_2O_2 capability test showed excellent anti-H_2O_2 capability of these nanococktails. In this part, *in vitro* cell-based anti-ROS studies were conducted to evaluate the scavenging of general ROS in LPS-stimulated macrophages. In our anti-ROS efficacy studies, macrophages were chosen to be the cell model as they have been reported as a major ROS-producing cell in many ROS and inflammatory-related diseases.[57] LPS was selected as a stimulant in macrophages because it has been well studied and widely used as an accelerator of internal ROS such as H_2O_2 and superoxide.[58] Lipopolysaccharide from the photosynthetic bacterium Rhodobacter sphaeroides (LPS-RS) was utilized as the inhibitor of the LPS by targeting the toll-like receptor 4. In this ROS scavenging study, macrophage cells were incubated with LPS and different nanoparticles overnight in different concentrations of cerium, followed by treatment with DCF-DA for 10 min. ROS inside the cells were measured by the fluorescence intensity of 2', 7' −dichlorofluorescein (DCF). A PerkinElmer plate reader measured the fluorescence intensity, and fluorescence images were taken using fluorescence microscopy. Cells treated with Chit-IOCO nanoparticles displayed a distinct reduction of ROS (21%) when the concentration of cerium increased above 1 μg/mL. The eventual ROS level of cells treated with Chit-IOCO at 10 μg/mL of cerium was nearly the same as control cells without LPS stimulation (100% scavenging) and LPS-RS group (Figure 8A(i)).

Chit-TPP-IOCO began to show a notable ROS scavenging ability at a cerium concentration of 0.5 μg/mL or above (Figure 8A(ii)). When the concentration of cerium of Chit-TPP-IOCO was higher than 1 μg/mL, the ROS level of the LPS-stimulated macrophages was close to those non-LPS-treated cells. However, the low ROS level observed in macrophages treated with Chit-TPP-IOCO at higher concentrations ([Ce] above 5 μg/mL) might be related to its cytotoxicity (Figure 7). Nevertheless, the anti-ROS capability of Chit-TPP-IOCO is nondebatable because at low concentrations ([Ce] below 5 μg/mL) where its cytotoxicity was not detected, Chit-TPP-IOCO exhibited efficient anti-ROS activity. Images acquired from the fluorescence microscope (Figure 8B) demonstrated that the macrophages treated with the nanococktails had a fluorescence intensity similar to that of the cell control group, which was much lower than that in the macrophages stimulated with LPS. Therefore, these results demonstrated the promising ROS scavenging abilities of both Chit-IOCO and Chit-TPP-IOCO cocktail.

The ROS scavenging of the nanococktails was attributed to the cerium oxide nanoparticles. As mentioned above, the anti-ROS effect of cerium oxide is affected by surface valence. Cerium can exist in two oxidation states: trivalence Ce^{3+} and tetravalence Ce^{4+}. The proportion of surface trivalent cerium has a significant influence on the anti-ROS effect of cerium oxide.[22] It was reported that nanoceria with approximately 22% of the trivalent cerium on its surface offered better antioxidant properties in comparison with 40% of the trivalent cerium.[22,59] Correspondingly, the nanoceria used in our nanococktails have a similar ratio of Ce^{3+}/Ce^{4+} at around 1/4 or 20% of Ce^{3+}which demonstrated effective anti-ROS ability in macrophages.

Previous studies have also confirmed the antioxidant activity of nanocerias.[60] Schubert *et al.*[61,62] first reported that nanocerias were capable of increasing the viability of the hydrogen peroxide-treated rat hippocampal nerve cells and human breast fibrosarcoma cells. Hirst *et al.*[19] then showed that their nanoceria (5 nm) at the concentration around 1.4 μg/mL of cerium could significantly reduce almost 100% the ROS level in the LPS-stimulated J774A.1 macrophage. Furthermore, Xia *et al.*[63] also tested the anti-ROS effect of nanoceria in diesel exhaust particle-stimulated RAW 264 cells. Their results indicated that nanoceria at the concentration of 20.35 μg Ce/mL scavenged around 40% of ROS in the cells. However, no anti-ROS ability of these nanoceria was reported at the concentration of 1 μg Ce/mL. In 2018, Chen and Xu[64] investigated the anti-ROS ability of different concentrations of cerium oxide nanoparticles in the LPS-treated RAW 264 macrophage. Their results indicated that their nanocerias at a size of 285 nm did not have distinct anti-ROS ability until the concentration of the cerium reached 81.4 μg/mL. In our

https://doi.org/10.1021/acsanm.1c00141
ACS Appl. Nano Mater. XXXX, XXX, XXX−XXX

current study, the nanococktails exhibited ROS scavenging effect efficiently at a lower Ce concentration (1 μg/mL) in LPS-treated J774A.1 cells compared to studies discussed above. At 1 μg Ce/mL, Chit-IOCO scavenged 21% ROS while Chit-TPP-IOCO reduced almost 100% ROS. Overall, Chit-IOCO and Chit-TPP-IOCO nanococktails demonstrated excellent anti-ROS scavenging ability in macrophages.

3.7.2. Macrophage MRI Capability. Iron oxide nanoparticles are a safe, reliable, and effective MRI contrast agent and also show great potential in the diagnosis of various diseases.[29−40,42−44,65−68] It is also widely used as an MRI imaging component in theranostic nanoparticles for cancer and inflammatory diseases.[69,70] Recently, iron oxide nanoparticles in combination with high-density lipoproteins[71] and prostacyclin[72] have been reported as the theranostic nanoparticles for atherosclerosis. Previous results (Figure 6) showed that both Chit-IOCO and Chit-TPP-IOCO are reliable contrast agents for MRI. The efficacy of macrophages labelled with Chit-IOCO and Chit-TPP-IOCO as MRI contrast agents was assessed using J774A.1 cells incubated with nanoparticles for 24 h prior to MRI. Macrophages labelled with Chit-IOCO displayed a strong MRI T_2 effect at an iron concentration of 29.6 μg/mL (Figure 9A,C). At a similar iron concentration, macrophages treated with Chit-TPP-IOCO showed only slightly higher relaxation rates than the nontreated group (Figure 9B,D). Hence, significant MRI signal enhancement cannot be observed in Chit-TPP-IOCO-treated macrophages. This is due to the weaker T_2-weighted relaxivity of Chit-TPP-IOCO demonstrated in Figure 6B,C. Hence, the MRI signal of Chit-TPP-IOCO is weaker at similar iron concentrations. Overall, these results clearly demonstrate that Chit-IOCO is more effective than Chit-TPP-IOCO as MRI contrast agents in macrophages.

Our data shows that the developed nanococktails could provide both anti-ROS ability for treatment and MRI capability for detection (diagnosis) in one dose, confirming their potential theranostic aspect. It was also demonstrated that Chit-IOCO performed better than Chit-TPP-IOCO in general. The results also imply that it is possible to detect the uptake of the developed nanomaterials by MRI. Therefore, it would be feasible to track the delivery and distribution of the materials or ceria, the therapeutic component in these systems, via MRI *in vivo*.

4. CONCLUSIONS

In this study, we investigated the feasibility to develop chitosan nanoparticles containing IO and CO for ROS-related theranostics. Two different approaches were employed, where Chit-IOCO and Chit-TPP-IOCO nanococktails were successfully synthesized with nanoceria as the therapeutic module and SPIONs as the imaging module. Characterization data showed that the sizes of these nanococktails were 153 and 125 nm, respectively, with a low PDI (less than 0.2). *In vitro* toxicity studies showed that Chit-IOCO had lower cytotoxicity for macrophages than Chit-TPP-IOCO. MRI measurements demonstrated that Chit-IOCO is a superior contrast agent of MRI than Chit-TPP-IOCO. Nonetheless, results indicated that both Chit-IOCO and Chit-TPP-IOCO nanoparticles display effective anti-ROS behavior in the solution and in LPS-treated macrophages. The excellent anti-ROS capacity of our Chit-IOCO and Chit-TPP-IOCO nanococktails was due to the appropriate proportioning of Ce^{3+}. Taken all together, it was concluded that the nanococktail synthesized by the electrostatic self-assembly method (Chit-IOCO) performed better than the one synthesized by ionic gelation (Chit-TPP-IOCO).

Overall, we have established that Chit-IOCO as a theranostic modular nanococktail can be utilized as a potential platform for the simultaneous treatment and diagnosis of ROS-related diseases in one dose. This research also put forward the concept of modular nanoparticles. To achieve the aim of theranostic nanoparticles in this study, we included CO-TSC and IO-TPP as the treatment and diagnosis modules in this modular nanoplatform. These, however, can be changed depending on the purposes and requirements of future personalized medicine. The loading of the modules can also be adjusted easily. The synthesis procedure of these nanococktails is relatively simple, allowing the advantage for future scale up and potential clinical translation. Moreover, the nanococktails can be further modified to specifically target ROS-related cells such as macrophages. In the future, we will test the anti-inflammatory activity of these newly developed nanococktails in activated macrophages as it was shown in previous studies that cerium oxide could reduce inflammation. Further studies on *in vivo* anti-inflammatory activity will also be conducted. The developed nanococktails containing both cerium oxide and iron oxide nanoparticles have great potential for simultaneous therapy and detection of ROS-related and inflammatory diseases such as atherosclerosis and rheumatoid arthritis.

■ ASSOCIATED CONTENT

Supporting Information

The Supporting Information is available free of charge at https://pubs.acs.org/doi/10.1021/acsanm.1c00141.

Schematic illustration of the preparation of phantom vessel for MRI; assessment of the stability of CO-TSC in water for 24 h; characteristics of Chit-TPP; and FTIR spectroscopy of nanoparticles and their relevant materials (PDF)

■ AUTHOR INFORMATION

Corresponding Author

Hang T. Ta − *Queensland Micro- and Nanotechnology, Griffith University, Nathan, Queensland 4111, Australia; Australian Institute for Bioengineering and Nanotechnology, University of Queensland, St Lucia, Queensland 4072, Australia; School of Environment and Science, Griffith University, Nathan, Queensland 4111, Australia;* orcid.org/0000-0003-1188-0472; Email: h.ta@griffith.edu.au

Authors

Yuao Wu − *Australian Institute for Bioengineering and Nanotechnology, University of Queensland, St Lucia, Queensland 4072, Australia; Queensland Micro- and Nanotechnology, Griffith University, Nathan, Queensland 4111, Australia*

Run Zhang − *Australian Institute for Bioengineering and Nanotechnology, University of Queensland, St Lucia, Queensland 4072, Australia;* orcid.org/0000-0002-0943-824X

Huong D. N. Tran − *Australian Institute for Bioengineering and Nanotechnology, University of Queensland, St Lucia, Queensland 4072, Australia; Queensland Micro- and*

https://doi.org/10.1021/acsanm.1c00141
ACS Appl. Nano Mater. XXXX, XXX, XXX−XXX

Nanotechnology, Griffith University, Nathan, Queensland 4111, Australia

Nyoman D. Kurniawan − *Centre of Advanced Imaging, University of Queensland, St Lucia, Queensland 4072, Australia*

Shehzahdi S. Moonshi − *Australian Institute for Bioengineering and Nanotechnology, University of Queensland, St Lucia, Queensland 4072, Australia*

Andrew K. Whittaker − *Australian Institute for Bioengineering and Nanotechnology, University of Queensland, St Lucia, Queensland 4072, Australia; ARC Centre of Excellence in Convergent Bio-Nano Science and Technology, The University of Queensland, Brisbane, Queensland 4072, Australia;* orcid.org/0000-0002-1948-8355

Complete contact information is available at: https://pubs.acs.org/10.1021/acsanm.1c00141

Notes

The authors declare no competing financial interest.

■ ACKNOWLEDGMENTS

This work is funded by the National Health and Medical Research Council (HTT: APP1037310, APP1182347, and APP2002827) and Heart Foundation (HTT: 102761). The authors would like to acknowledge the Australian National Fabrication Facility (Queensland Node) and the National Imaging Facility, Centre for Advanced Imaging for access to key items of equipment.

■ REFERENCES

(1) Apel, K.; Hirt, H. Reactive oxygen species: metabolism, oxidative stress, and signal transduction. *Annu. Rev. Plant Biol.* **2004**, *55*, 373−399.

(2) Turrens, J. F. Mitochondrial formation of reactive oxygen species. *J. Physiol.* **2003**, *552*, 335−344.

(3) Alfadda, A. A.; Sallam, R. M. Reactive oxygen species in health and disease. *J. Biomed. Biotechnol.* **2012**, *2012*, 936486.

(4) Phaniendra, A.; Jestadi, D. B.; Periyasamy, L. Free radicals: properties, sources, targets, and their implication in various diseases. *Indian J. Clin. Biochem.* **2015**, *30*, 11−26.

(5) Forrester, S. J.; Kikuchi, D. S.; Hernandes, M. S.; Xu, Q.; Griendling, K. K. Reactive oxygen species in metabolic and inflammatory signaling. *Circ. Res.* **2018**, *122*, 877−902.

(6) Kattoor, A. J.; Pothineni, N. V. K.; Palagiri, D.; Mehta, J. L. Oxidative stress in atherosclerosis. *Curr. Atheroscler. Rep.* **2017**, *19*, 42.

(7) Cichoń, N.; Lach, D.; Dziedzic, A.; Bijak, M.; Saluk, J. The inflammatory processes in atherogenesis. *Pol. Merkuriusz Lek.* **2017**, *42*, 125−128.

(8) Afroz, R.; Cao, Y.; Rostam, M. A.; Ta, H.; Xu, S.; Zheng, W.; Osman, N.; Kamato, D.; Little, P. J. Signalling pathways regulating galactosaminoglycan synthesis and structure in vascular smooth muscle: implications for lipoprotein binding and atherosclerosis. *Pharmacol. Ther.* **2018**, *187*, 88−97.

(9) Mateen, S.; Moin, S.; Khan, A. Q.; Zafar, A.; Fatima, N. Increased reactive oxygen species formation and oxidative stress in rheumatoid arthritis. *PLoS One* **2016**, *11*, No. e0152925.

(10) Mittal, M.; Siddiqui, M. R.; Tran, K.; Reddy, S. P.; Malik, A. B. Reactive Oxygen Species in Inflammation and Tissue Injury. *Antioxid. Redox Signaling* **2014**, *20*, 1126−1167.

(11) Curi, R.; de Siqueira Mendes, R.; de Campos Crispin, L. A.; Norata, G. D.; Sampaio, S. C.; Newsholme, P. A past and present overview of macrophage metabolism and functional outcomes. *Clin. Sci.* **2017**, *131*, 1329−1342.

(12) Rajagopalan, S.; Meng, X. P.; Ramasamy, S.; Harrison, D. G.; Galis, Z. S. Reactive oxygen species produced by macrophage-derived foam cells regulate the activity of vascular matrix metalloproteinases in vitro. Implications for atherosclerotic plaque stability. *J. Clin. Invest.* **1996**, *98*, 2572−2579.

(13) Montecucco, F.; Mach, F. Atherosclerosis is an inflammatory disease. *Semin. Immunopathol.* **2009**, *31*, 1−3.

(14) Furie, B.; Furie, B. C. Mechanisms of thrombus formation. *N. Engl. J. Med.* **2008**, *359*, 938−949.

(15) Sareila, O.; Hagert, C.; Kelkka, T.; Linja, M.; Xu, B.; Kihlberg, J.; Holmdahl, R. Reactive oxygen species regulate both priming and established arthritis, but with different mechanisms. *Antioxid. Redox Signaling* **2017**, *27*, 1473−1490.

(16) Kładna, A.; Aboul-Enein, H. Y.; Kruk, I.; Lichszteld, K.; Michalska, T. Scavenging of reactive oxygen species by some nonsteroidal anti-inflammatory drugs and fenofibrate. *Biopolymers* **2006**, *82*, 99−105.

(17) López-Alarcón, C.; Denicola, A. Evaluating the antioxidant capacity of natural products: A review on chemical and cellular-based assays. *Anal. Chim. Acta* **2013**, *763*, 1−10.

(18) Carocho, M.; Ferreira, I. C. F. R. A review on antioxidants, prooxidants and related controversy: natural and synthetic compounds, screening and analysis methodologies and future perspectives. *Food Chem. Toxicol.* **2013**, *51*, 15−25.

(19) Hirst, S. M.; Karakoti, A. S.; Tyler, R. D.; Sriranganathan, N.; Seal, S.; Reilly, C. M. Anti-inflammatory properties of cerium oxide nanoparticles. *Small* **2009**, *5*, 2848−2856.

(20) Hirst, S. M.; Karakoti, A.; Singh, S.; Self, W.; Tyler, R.; Seal, S.; Reilly, C. M. Bio-distribution andin vivoantioxidant effects of cerium oxide nanoparticles in mice. *Environ. Toxicol. Pharmacol.* **2013**, *28*, 107−118.

(21) Teterin, Y. A.; Teterin, A. Y.; Lebedev, A. M.; Utkin, I. O. The XPS spectra of cerium compounds containing oxygen. *J. Electron Spectrosc. Relat. Phenom.* **1998**, *88*−*91*, 275−279.

(22) Korsvik, C.; Patil, S.; Seal, S.; Self, W. T. Superoxide dismutase mimetic properties exhibited by vacancy engineered ceria nanoparticles. *Chem. Commun.* **2007**, *10*, 1056−1058.

(23) Chaudhury, K.; Babu K, N.; Singh, A. K.; Das, S.; Kumar, A.; Seal, S. Mitigation of endometriosis using regenerative cerium oxide nanoparticles. *Nanomedicine* **2013**, *9*, 439−448.

(24) Clark, A.; Zhu, A.; Sun, K.; Petty, H. R. Cerium oxide and platinum nanoparticles protect cells from oxidant-mediated apoptosis. *J. Nanopart. Res.* **2011**, *13*, 5547−5555.

(25) Yan, K. C.; Sedgwick, A. C.; Zang, Y.; Chen, G. R.; He, X. P.; Li, J.; Yoon, J.; James, T. D. Sensors, imaging agents, and theranostics to help understand and treat reactive oxygen species related diseases. *Small Methods* **2019**, *3*, 1900013.

(26) Ta, H. T.; Li, Z.; Wu, Y.; Cowin, G.; Zhang, S.; Yago, A.; Whittaker, A. K.; Xu, Z. P. Effects of magnetic field strength and particle aggregation on relaxivity of ultra-small dual contrast iron oxide nanoparticles. *Mater. Res. Express* **2017**, *4*, 116105.

(27) Vazquez-Prada, K. X.; Lam, J.; Kamato, D.; Xu, Z. P.; Little, P. J.; Ta, H. T. Targeted Molecular Imaging of Cardiovascular Diseases by Iron Oxide Nanoparticles. *Arterioscler., Thromb., Vasc. Biol.* **2021**, *41*, 601−613.

(28) Wang, Y.-X. J.; Hussain, S. M.; Krestin, G. P. Superparamagnetic iron oxide contrast agents: physicochemical characteristics and applications in MR imaging. *Eur. Radiol.* **2001**, *11*, 2319−2331.

(29) Ta, H. T.; Arndt, N.; Wu, Y.; Lim, H. J.; Landeen, S.; Zhang, R.; Kamato, D.; Little, P. J.; Whittaker, A. K.; Xu, Z. P. Activatable magnetic resonance nanosensor as a potential imaging agent for detecting and discriminating thrombosis. *Nanoscale* **2018**, *10*, 15103−15115.

(30) Liu, Y.; Wu, Y.; Zhang, R.; Lam, J.; Ng, J. C.; Xu, Z. P.; Li, L.; Ta, H. T. Investigating the use of layered double hydroxide nanoparticles as carriers of metal oxides for theranostics of ROS-related diseases. *ACS Appl. Bio Mater.* **2019**, *2*, 5930−5940.

(31) Ta, H.; Li, Z.; Hagemeyer, C.; Cowin, G.; Palasubramaniam, J.; Peter, K.; Whittaker, A. Self-confirming molecular imaging of activated platelets via iron oxide nanoparticles displaying unique dual MRI contrast. *Atherosclerosis* **2017**, *263*, No. e146.
(32) Arndt, N.; Tran, H. D. N.; Zhang, R.; Xu, Z. P.; Ta, H. T. Different approaches to develop nanosensors for diagnosis of diseases. *Adv. Sci.* **2020**, *7*, 2001476.
(33) Zhang, Y.; Koradia, A.; Kamato, D.; Popat, A.; Little, P. J.; Ta, H. T. Treatment of atherosclerotic plaque: perspectives on theranostics. *J. Pharm. Pharmacol.* **2019**, *71*, 1029−1043.
(34) Ta, H. T.; Li, Z.; Hagemeyer, C. E.; Cowin, G.; Zhang, S.; Palasubramaniam, J.; Alt, K.; Wang, X.; Peter, K.; Whittaker, A. K. Molecular imaging of activated platelets via antibody-targeted ultra-small iron oxide nanoparticles displaying unique dual MRI contrast. *Biomaterials* **2017**, *134*, 31−42.
(35) Zia, A.; Wu, Y.; Nguyen, T.; Wang, X.; Peter, K.; Ta, H. T. The choice of targets and ligands for site-specific delivery of nanomedicine to atherosclerosis. *Cardiovasc. Res.* **2020**, *116*, 2055−2068.
(36) Ta, H.; Prabhu, S.; Leitner, E.; Jia, F.; Putnam, K.; Bassler, N.; Peter, K.; Hagemeyer, C. Targeted molecular imaging and cell homing in cardiovascular disease via antibody-sortagging. *Atherosclerosis* **2015**, *241*, No. e26.
(37) Hagemeyer, C. E.; Alt, K.; Johnston, A. P. R.; Such, G. K.; Ta, H. T.; Leung, M. K. M.; Prabhu, S.; Wang, X.; Caruso, F.; Peter, K. Particle generation, functionalization and sortase A-mediated modification with targeting of single-chain antibodies for diagnostic and therapeutic use. *Nat. Protoc.* **2015**, *10*, 90−105.
(38) Ta, H. T.; Prabhu, S.; Leitner, E.; Jia, F.; von Elverfeldt, D.; Jackson, K. E.; Heidt, T.; Nair, A. K. N.; Pearce, H.; von zur Muhlen, C.; Wang, X.; Peter, K.; Hagemeyer, C. E. Enzymatic single-chain antibody tagging: a universal approach to targeted molecular imaging and cell homing in cardiovascular disease. *Circ. Res.* **2011**, *109*, 365−373.
(39) Yusof, N. N. M.; McCann, A.; Little, P. J.; Ta, H. T. Non-invasive imaging techniques for the differentiation of acute and chronic thrombosis. *Thromb. Res.* **2019**, *177*, 161−171.
(40) Ta, H. T.; Peter, K.; Hagemeyer, C. E. Enzymatic antibody tagging: toward a universal biocompatible targeting tool. *Trends Cardiovasc. Med.* **2012**, *22*, 105−111.
(41) Ta, H. T.; Prabhu, S.; Leitner, E.; Jia, F.; Putnam, K.; Bassler, N.; Peter, K.; Hagemeyer, C. Late-Breaking Basic Science Abstracts From the American Heart Association's Scientific Sessions 2010, Chicago, Illinois, November 13−17, 2010. *Circ. Res.* **2010**, *107*, e32−e40.
(42) Ta, H.; Prabhu, S.; Leitner, E.; Putnam, K.; Jia, F.; Bassler, N.; Peter, K.; Hagemeyer, C. A novel biotechnological approach for targeted regenerative cell therapy and molecular imaging of atherothrombosis. *Heart, Lung Circ.* **2010**, *19*, S10.
(43) Zhang, Z.-Q.; Song, S.-C. Thermosensitive/superparamagnetic iron oxide nanoparticle-loaded nanocapsule hydrogels for multiple cancer hyperthermia. *Biomaterials* **2016**, *106*, 13−23.
(44) Wang, D.; Fei, B.; Halig, L. V.; Qin, X.; Hu, Z.; Xu, H.; Wang, Y. A.; Chen, Z.; Kim, S.; Shin, D. M.; Chen, Z. Targeted iron-oxide nanoparticle for photodynamic therapy and imaging of head and neck cancer. *ACS Nano* **2014**, *8*, 6620−6632.
(45) Kumar, M. N. V. R.; Muzzarelli, R. A. A.; Muzzarelli, C.; Sashiwa, H.; Domb, A. J. Chitosan chemistry and pharmaceutical perspectives. *Chem. Rev.* **2004**, *104*, 6017−6084.
(46) Singh, N.; Jenkins, G. J. S.; Asadi, R.; Doak, S. H. Potential toxicity of superparamagnetic iron oxide nanoparticles (SPION). *Nano Rev.* **2010**, *1*, 5358.
(47) Lam, T.; Pouliot, P.; Avti, P. K.; Lesage, F.; Kakkar, A. K. Superparamagnetic iron oxide based nanoprobes for imaging and theranostics. *Adv. Colloid Interface Sci.* **2013**, *199*−*200*, 95−113.
(48) Liu, X.; Wei, W.; Yuan, Q.; Zhang, X.; Li, N.; Du, Y.; Ma, G.; Yan, C.; Ma, D. Apoferritin-CeO2nano-truffle that has excellent artificial redox enzyme activity. *Chem. Commun.* **2012**, *48*, 3155−3157.
(49) Karakoti, A.; Singh, S.; Dowding, J. M.; Seal, S.; Self, W. T. Redox-active radical scavenging nanomaterials. *Chem. Soc. Rev.* **2010**, *39*, 4422−4432.
(50) Elahi, N.; Kamali, M.; Baghersad, M. H. Recent biomedical applications of gold nanoparticles: A review. *Talanta* **2018**, *184*, 537−556.
(51) Gan, Q.; Wang, T.; Cochrane, C.; McCarron, P. Modulation of surface charge, particle size and morphological properties of chitosan-TPP nanoparticles intended for gene delivery. *Colloids Surf., B* **2005**, *44*, 65−73.
(52) Katas, H.; Alpar, H. O. Development and characterisation of chitosan nanoparticles for siRNA delivery. *J. Controlled Release* **2006**, *115*, 216−225.
(53) Loutfy, S. A.; El-Din, H. M. A.; Elberry, M. H.; Allam, N. G.; Hasanin, M. T. M.; Abdellah, A. M. Synthesis, characterization and cytotoxic evaluation of chitosan nanoparticles: in vitro liver cancer model. *Adv. Nat. Sci.: Nanosci. Nanotechnol.* **2016**, *7*, 035008.
(54) Hajesmaeelzadeh, F.; Shanehsazzadeh, S.; Grüttner, C.; Daha, F. J.; Oghabian, M. A. Effect of coating thickness of iron oxide nanoparticles on their relaxivity in the MRI. *Iran. J. Basic Med. Sci.* **2016**, *19*, 166.
(55) Korchinski, D. J.; Taha, M.; Yang, R.; Nathoo, N.; Dunn, J. F. Iron Oxide as an MRI Contrast Agent for Cell Tracking. *Magn. Reson. Insights* **2015**, *8*, 15−29.
(56) Moore, K. J.; Tabas, I. Macrophages in the pathogenesis of atherosclerosis. *Cell* **2011**, *145*, 341−355.
(57) Shirai, T.; Hilhorst, M.; Harrison, D. G.; Goronzy, J. J.; Weyand, C. M. Macrophages in vascular inflammation - From atherosclerosis to vasculitis. *Autoimmunity* **2015**, *48*, 139−151.
(58) Hsu, H.-Y.; Wen, M.-H. Lipopolysaccharide-mediated reactive oxygen species and signal transduction in the regulation of interleukin-1 gene expression. *J. Biol. Chem.* **2002**, *277*, 22131−22139.
(59) Das, M.; Patil, S.; Bhargava, N.; Kang, J.-F.; Riedel, L. M.; Seal, S.; Hickman, J. J. Auto-catalytic ceria nanoparticles offer neuroprotection to adult rat spinal cord neurons. *Biomaterials* **2007**, *28*, 1918−1925.
(60) Nelson, B.; Johnson, M.; Walker, M.; Riley, K.; Sims, C. Antioxidant cerium oxide nanoparticles in biology and medicine. *Antioxidants* **2016**, *5*, 15.
(61) Schubert, D.; Dargusch, R.; Raitano, J.; Chan, S.-W. Cerium and yttrium oxide nanoparticles are neuroprotective. *Biochem. Biophys. Res. Commun.* **2006**, *342*, 86−91.
(62) Clark, A.; Zhu, A.; Sun, K.; Petty, H. R. Cerium oxide and platinum nanoparticles protect cells from oxidant-mediated apoptosis. *J. Nanopart. Res.* **2011**, *13*, 5547.
(63) Xia, T.; Kovochich, M.; Liong, M.; Mädler, L.; Gilbert, B.; Shi, H.; Yeh, J. I.; Zink, J. I.; Nel, A. E. Comparison of the mechanism of toxicity of zinc oxide and cerium oxide nanoparticles based on dissolution and oxidative stress properties. *ACS Nano* **2008**, *2*, 2121−2134.
(64) Chen, G.; Xu, Y. Biosynthesis of cerium oxide nanoparticles and their effect on lipopolysaccharide (LPS) induced sepsis mortality and associated hepatic dysfunction in male Sprague Dawley rats. *Mater. Sci. Eng. C* **2018**, *83*, 148−153.
(65) Zhu, M.-T.; Wang, B.; Wang, Y.; Yuan, L.; Wang, H.-J.; Wang, M.; Ouyang, H.; Chai, Z.-F.; Feng, W.-Y.; Zhao, Y.-L. Endothelial dysfunction and inflammation induced by iron oxide nanoparticle exposure: Risk factors for early atherosclerosis. *Toxicol. Lett.* **2011**, *203*, 162−171.
(66) Kedziorek, D. A.; Kraitchman, D. L. Superparamagnetic iron oxide labeling of stem cells for MRI tracking and delivery in cardiovascular disease. *Stem Cells for Myocardial Regeneration*; Springer, 2010; pp 171−183.
(67) Riegler, J.; Liew, A.; Hynes, S. O.; Ortega, D.; O'Brien, T.; Day, R. M.; Richards, T.; Sharif, F.; Pankhurst, Q. A.; Lythgoe, M. F. Superparamagnetic iron oxide nanoparticle targeting of MSCs in vascular injury. *Biomaterials* **2013**, *34*, 1987−1994.
(68) Ta, H. T.; Prabhu, S.; Leitner, E.; Jia, F.; Putnam, K.; Bassler, N.; Peter, K.; Hagemeyer, C. Antibody-sortagging: a universal

https://doi.org/10.1021/acsanm.1c00141
ACS Appl. Nano Mater. XXXX, XXX, XXX−XXX

approach towards targeted molecular imaging and cell homing in cardiovascular disease. *Circ. Res.* **2010**, *107*, e37−e38.
(69) Dadfar, S. M.; Roemhild, K.; Drude, N. I.; von Stillfried, S.; Knüchel, R.; Kiessling, F.; Lammers, T. Iron oxide nanoparticles: Diagnostic, therapeutic and theranostic applications. *Adv. Drug Delivery Rev.* **2019**, *138*, 302−325.
(70) Xie, J.; Jon, S. Magnetic nanoparticle-based theranostics. *Theranostics* **2012**, *2*, 122.
(71) Nandwana, V.; Ryoo, S.-R.; Kanthala, S.; McMahon, K. M.; Rink, J. S.; Li, Y.; Venkatraman, S. S.; Thaxton, C. S.; Dravid, V. P. High-density lipoprotein-like magnetic nanostructures (HDL-MNS): theranostic agents for cardiovascular disease. *Chem. Mater.* **2017**, *29*, 2276−2282.
(72) Oumzil, K.; Ramin, M. A.; Lorenzato, C.; Hémadou, A.; Laroche, J.; Jacobin-Valat, M. J.; Mornet, S.; Roy, C.-E.; Kauss, T.; Gaudin, K.; Clofent-Sanchez, G.; Barthélémy, P. Solid lipid nanoparticles for image-guided therapy of atherosclerosis. *Bioconjugate Chem.* **2016**, *27*, 569−575.

https://doi.org/10.1021/acsanm.1c00141
ACS Appl. Nano Mater. XXXX, XXX, XXX−XXX

Chitosan Nano-cocktails Containing Both Ceria and Superparamagnetic Iron Oxide Nanoparticles for Reactive Oxygen Species-Related Theranostics

Yuao Wu[1,2], Run Zhang[1], Huong D.N. Tran[1,2], Nyoman D. Kurniawan[4], Shehzahdi S. Moonshi[1], Andrew K. Whittaker[1,5], Hang T. Ta[1,2,3*]

[1]Australian Institute for Bioengineering and Nanotechnology, University of Queensland, St Lucia, Queensland 4072, Australia

[2]Queensland Micro- and Nanotechnology, Griffith University, Nathan, Queensland 4111, Australia

[3]School of Environment and Science, Griffith University, Nathan, Queensland 4111, Australia

[4]Centre of Advanced Imaging, University of Queensland, St Lucia, Queensland 4072, Australia

[5]ARC Centre of Excellence in Convergent Bio-Nano Science and Technology, The University of Queensland, Brisbane, Queensland 4072, Australia

*** Correspondence:** Hang T. Ta (h.ta@griffith.edu.au)

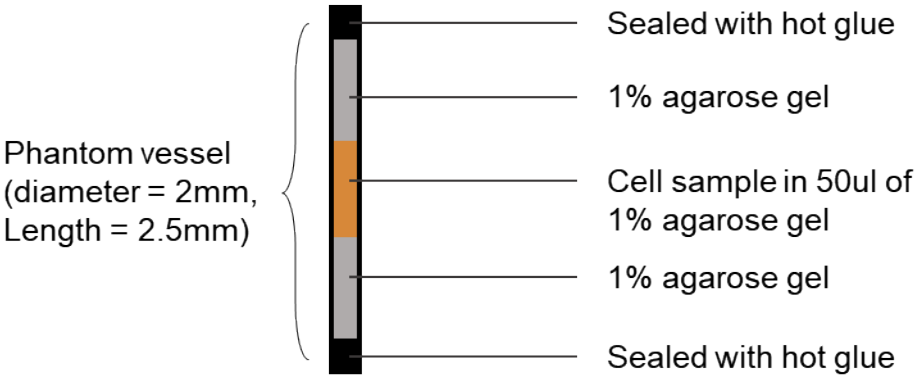

Scheme S1. Schematic Illustration of the Preparation of Phantom Vessel for MRI

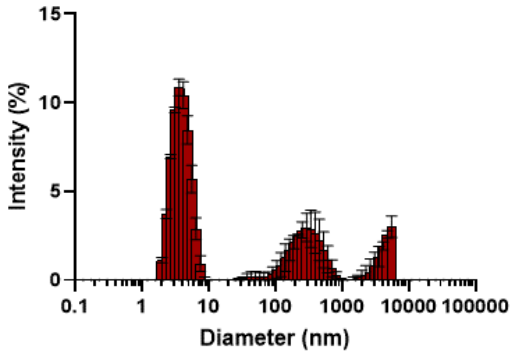

Fig S1. Assessment of the stability of CO-TSC in water for 24 hours. Size of CO-TSC in water solution was measured by DLS.

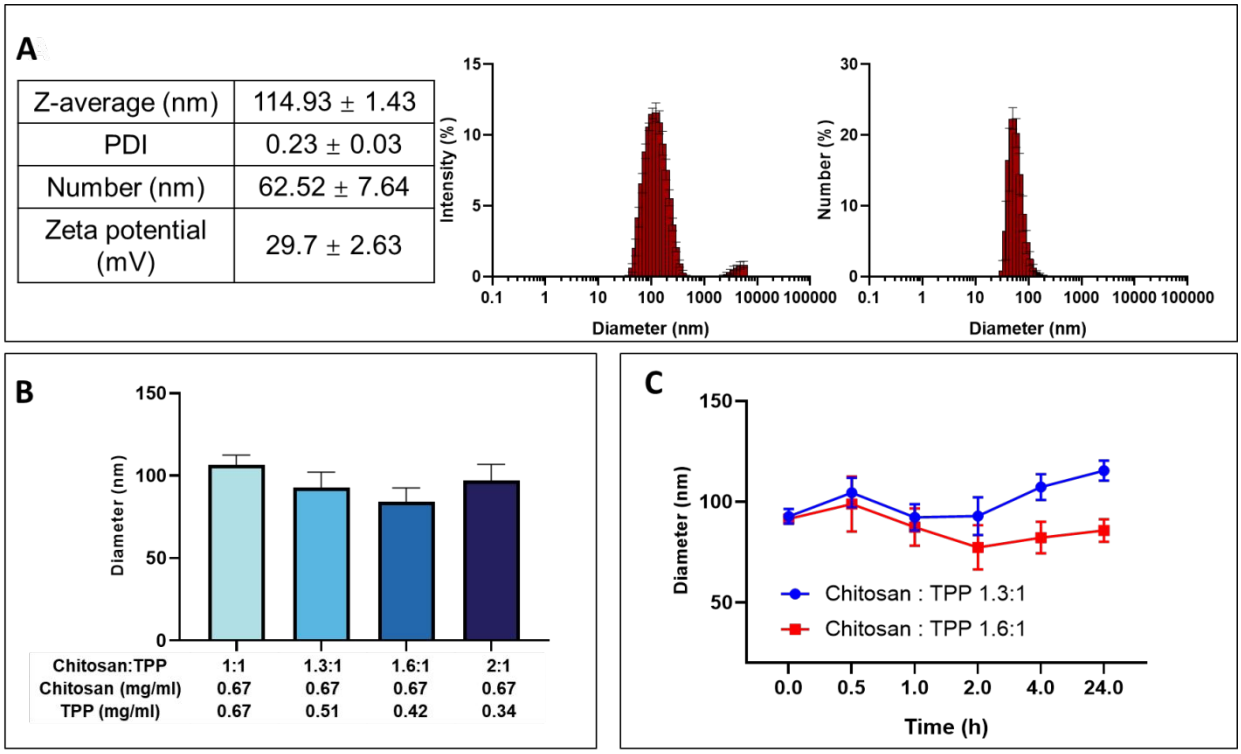

Fig S2. Characteristics of Chit-TPP. (A) Size and zeta potential of Chit-TPP measured by Zetasizer. Zeta potential data showed that Chit-TPP nanoparticle was positively charged. **(B)** DLS size distribution of the Chit-TPP nanoparticles. **(C)** Size of the Chit-TPP nanoparticles after synthesis with different concentrations of TPP. Different concentration of TPP in 2.5 ml of H_2O (0.67 mg/ml, 0.51 mg/ml, 0.42 mg/ml and 0.34 mg/ml) was pumping into 0.1% (w/w) of chitosan solution during synthesis. **(D)** Size of the Chit-TPP nanoparticles of different incubation time. Different concentration of TPP in 2.5 ml of H_2O (0.51 mg/ml), (0.42 mg/ml) was pumped into 0.1% (w/w) of chitosan solution (chitosan:TPP ratios of 1.3:1 and 1.6:1, respectively) and stirred for 0.5 h, 1 h, 2 h, 4 h, 24 h.

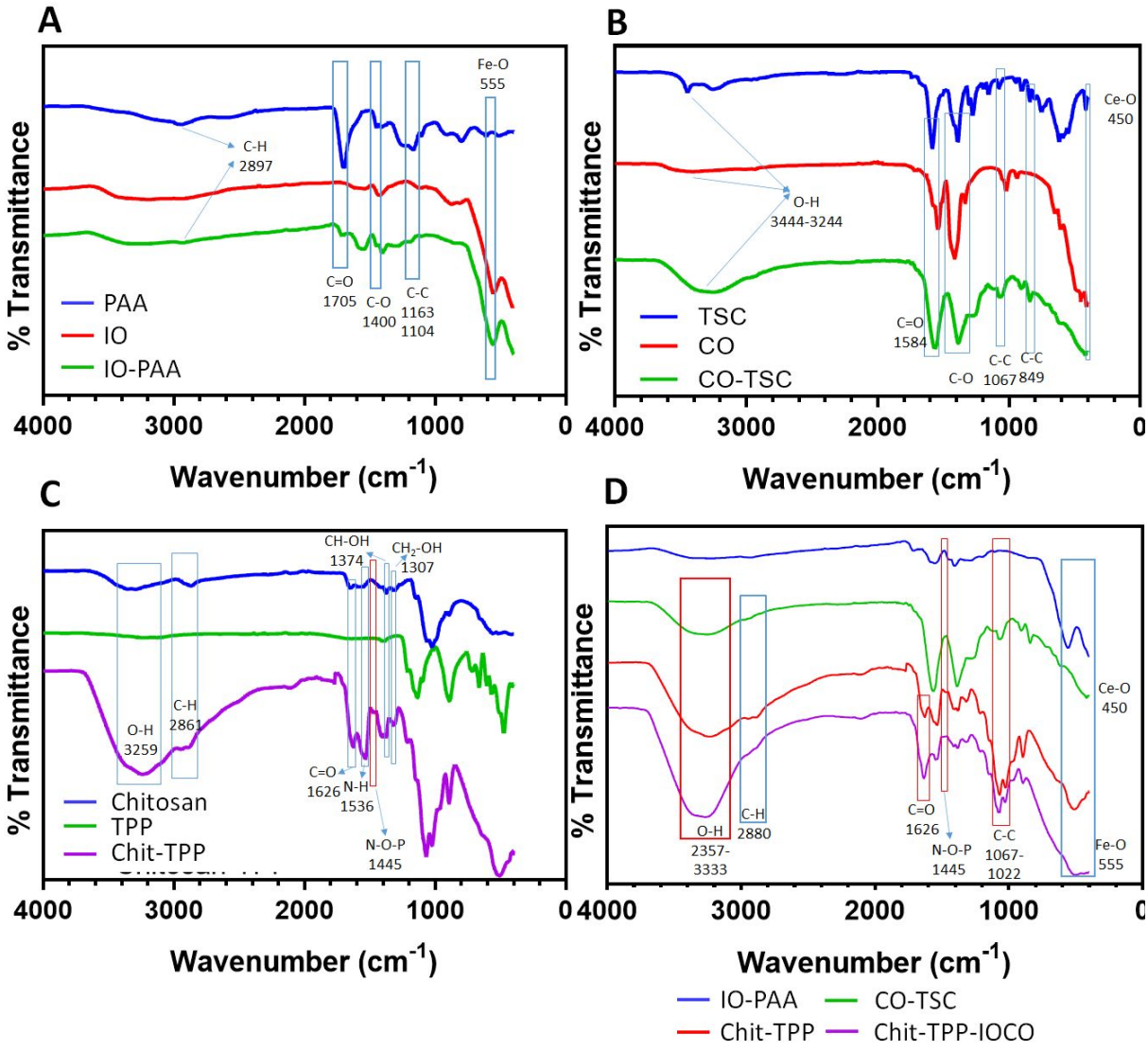

Fig S3. FTIR spectroscopy of nanoparticle and their relevant materials. (A) FTIR spectroscopy of PAA IO and IO-PAA. PAA, IO and IO-PAA powders were dried, followed by FTIR measurement. Peaks at around 2898 cm^{-1} showed C-H bonds, 1705 cm^{-1} indicated C=O bonds, 1400 cm^{-1} showed C-O bonds, 1104 to 1163 cm^{-1} showed C-C bonds and at 555 cm^{-1} were Fe-O bonds. According to the PAA and iron oxide structure and infrared spectroscopy, PAA was successfully coated on the IO-PAA nanoparticles. **(B)** FTIR spectroscopy of TSC, CO and CO-TSC. **(C)** FTIR spectroscopy of chitosan, TPP and Chit-TPP nanoparticle. **(D)** FTIR spectroscopy of IO-PAA, CO-TSC, Chit-TPP and Chit-TPP-IOCO nanoparticles.